Advances in Colloid and Interface Science 294 (2021) 102456

Contents lists available at ScienceDirect

Advances in Colloid and Interface Science

journal homepage: www.elsevier.com/locate/cis

Historical Perspective

# Composite materials based on heteroaggregated particles: Fundamentals and applications

Nizar B. Alsharif, Szabolcs Muráth, Bojana Katana, Istvan Szilagyi *

*MTA-SZTE Lendület Biocolloids Research Group, Interdisciplinary Excellence Center, Department of Physical Chemistry and Materials Science, University of Szeged, 1 Rerrich Béla tér, 6720 Szeged, Hungary*

ARTICLE INFO

*Keywords:*
Heteroaggregation
Nanostructure
Composite
Colloidal stability
Self-assembly

ABSTRACT

Homoaggregation of dispersed particles, i.e., aggregation of particles of the same shape, charge, size, and composition, is a well-studied field and various theoretical and experimental approaches exist to understand the major phenomena involved in such processes. Besides, heteroaggregation of particles, i.e., aggregation of particles of different shape, charge, size, or composition, has attracted widespread interest due to its relevance in various biomedical, industrial, and environmental systems. For instance, heteroaggregation of plastic contaminant particles with naturally occurring solid materials in waters (e.g., clays, silica and organic polymers) plays an important role in the decontamination technologies. Moreover, nanofabrication processes involving heteroaggregation of particles to prepare novel composite materials are widely implemented in fundamental science and in more applied disciplines. In such procedures, stable particle dispersions are mixed and the desired structure forms owing to the presence of interparticle forces of various origins, which can be tuned by performing appropriate surface functionalization as well as altering the experimental conditions. These composites are widely used in different fields from sensing through catalysis to biomedical delivery. The present review summarizes the recent progresses in the field including new findings regarding the basic principles in particle heteroaggregation, preparation strategies of heteroaggregated structures of different morphology, and the application of the obtained hybrid composites. Such information will be very helpful to those involved in the design of novel composites consisting of different nano or colloidal particles.

## 1. Introduction

Colloidal systems of nanostructured materials are constantly prone to dynamic changes such as aggregation, dissolution, sedimentation as well as chemical transformation [1–5]. While particles of stable colloids remain well separated and suspended, certain experimental conditions can induce homoaggregation (aggregation of the same particles), where particles approach each other and combine into large clusters leading to destabilization of the system [6]. Homoaggregation has been extensively studied and is now known to depend on numerous factors such as the pH, ionic strength, particle size, chemical composition, temperature, surface modification, the presence of naturally occurring organic matter or clays and the nature of the dispersion medium.

The Derjaguin-Landau-Verwey-Overbeek (DLVO) theory suggests that particle interactions and thus, the extent of homoaggregation is governed by relative contributions of two major interparticle forces, the attractive van der Waals as well as the repulsive electrostatic double layer forces. Accordingly, when the overall effect of the interplay among factors affecting aggregation results in attractive forces such as high ionic strength and large particles, the colloidal system tends to aggregate giving rise to instability. On the other hand, when conditions result in repulsive overall effect, such as highly protonated or deprotonated metal oxide nanoparticles, the particles remain separated from each other resulting in a stable colloidal system. Such ability to control particle aggregation has enabled the implementation of colloidal systems in numerous applications including food items such as dairy products [7], drug emulsions [3,8,9], wastewater purification [10], rubber industry [11], leather tanning [12], paint industry [13], paper and retention aids [14].

In multi-component colloidal systems, however, homoaggregation may occur concurrently along with heteroaggregation (aggregation among dissimilar particles) [15–17]. Heteroaggregation is a fundamental phenomenon in colloidal dispersions and occurs between components of different chemical composition, surface potential, charge,

* Corresponding author.
*E-mail address:* szistvan@chem.u-szeged.hu (I. Szilagyi).

https://doi.org/10.1016/j.cis.2021.102456
Received in revised form 27 May 2021;
Available online 31 May 2021

shape, or size [15,16,18]. Not only multi-components colloidal systems occur more frequently in nature such as water sources, soil, and river deltas [19–24], but also in many industrial applications including mineral flotation and coating [25,26]. Most importantly, heteroaggregation between nanostructured materials (e.g., nanospheres, nanoplates, or nanotubes) has been used as a synthetic route to prepare nanocomposites with diverse structures for numerous applications such as catalysis, drug delivery, water purification, artificial enzymes, and energy storage, among others [27–31].

In general, hybrids of different nanoparticles are highly functional materials with great potential in various applications such as catalysis [32], energy storage [33,34], electronics [35], sensing [36], water purification [37], drug delivery [38], therapeutic agents [39], and spacecraft protective coating [40], to name a few. Although these hybrid materials have been prepared via both in situ (synthesis of one component in the presence of the other) or ex situ heteroaggregation (simple mixing of dispersions of pre-synthesized particles), the sole focus of this review article is to report the progresses made on the latter strategy regarding both fundamental studies as well as advances in functional hybrid materials formation. The ex situ heteroaggregation, illustrated in Fig. 1, is more advantageous and allows rapid, convenient, and cost-effective syntheses that circumvent harsh temperature and pH conditions as well as tedious functionalization and surface modification procedures.

## 2. The heteroaggregation process: fundamental studies

Colloidal systems of dissimilar nanoparticles cannot be fully described with the DLVO theory [41,42]. As the case with homoaggregation, nevertheless, the heteroaggregation process in binary systems is driven by the existent attractive forces as well as the tendency of particles to minimize their surface energy. Also, the extent of repulsive interactions of electrostatic and steric origin as well as attractive van der Waals forces is tuned by altering the experimental conditions such as the pH and surface functionalization [43]. In binary systems, while DLVO forces of van der Waals and electrostatic exist among similar particles, there exist certain experimental conditions where additional (non-DLVO) attractive forces act between the different particles (e.g., oppositely charged particles) that lead to favourable interactions and subsequent heteroaggregation into various heteroaggregates with promising potential as functional composites. Moreover, only does heteroaggregation occur among differently shaped nanoparticles (sphere-sphere, sphere-tube, sphere-plate, rod-plate, etc.), but also between nanoparticles and naturally occurring inorganic, organic, biological colloids as well as viruses and bacteria [44–48]. The following subsections review the fundamental studies attempted to formulate an understanding of heteroaggregation based on the shape of the particles involved.

### 2.1. Sphere-sphere systems

During the heteroaggregation of spherical particles, the magnitude of the collective attractive (electrostatic and/or van der Waals) interparticle forces not only depends on the conditions in the medium such as the pH and the ionic strength, but also on the physicochemical properties of the particles themselves. Besides particle radius and interparticle distance, the van der Waals forces also depend on the Hamaker constant that manifests the inherent contribution of the nature, chemical composition, and the surface chemistry of the particles to the attractive forces. In addition, the particle size dependence tunes the aggregation regimes, where different types of interactions govern the aggregation process. For example, surface chemistry of particles similar in size significantly affect their homoaggregation, whereas in homoaggregation of differently sized particles, van der Waals forces play a major role, as their strength is proportional with the size of the particles [43]. On the other hand, heteroaggregation among either similarly or differently sized particles is governed by both the surface chemistry as well as DLVO type forces.

The fundamental features of heteroaggregation were explored in certain extent in the past due to the growing number of binary particle systems in various applications [48–52]. Extensive work has been carried out to fully understand heteroaggregation in multi-component dispersions, even though several aspects of heteroaggregation can be explained by DLVO. Hogg et al. presented the Hogg-Healy-Fuerstenau theory in 1965 to describe the kinetics of aggregation of binary colloidal systems. Using the Derjaguin and Debye-Hückel approximation for low surface potential, they derived a general expression that describes the potential energy of interaction between dissimilar particles and predicts the effect on system stability of parameters such as potential-determining ions, ionic strength, the particle size, and the relative presence of constituent particles [53]. Lopez-Lopez et al. reviewed the kinetic and structural aspects of theoretical and simulation advances on the heteroaggregation coupled with experimental work on the heteroaggregation of amidine and sulfate modified polystyrene latex (PS) particles in KBr electrolyte solutions [49]. In another review work, Lopez-Lopez et al. focused on electrostatically driven aggregation of

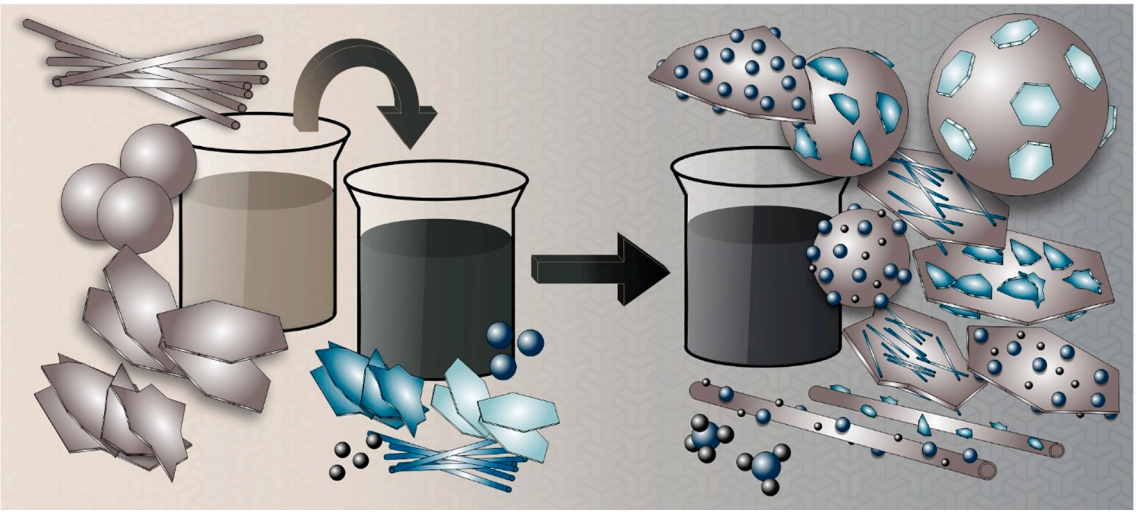

**Fig. 1.** Schematic illustration of ex situ heteroaggregation of particles of various sizes and shapes, where colloidal dispersions of pre-synthesized materials are simply mixed in the desired ratio.

binary systems of equally charged particles (symmetric system) using the same sulfate and amidine PS particles to carry out a detailed study on the heteroaggregation process and the colloidal stability over a wide range of electrolyte (KBr) concentration. The aggregation regimes as well as short and long-time aggregation kinetics were addressed from both experimental, theoretical and simulation point of view [16].

Studies were extended beyond simple symmetric systems. Trefalt et al. calculated the interaction forces and studied aggregation and deposition rates for asymmetric and symmetric systems as well as charged-neutral systems, based on the Poisson-Boltzmann model as well as the DLVO theory. The symmetry and charge regulation effects altered the heteroaggregation and deposition behaviour in such systems, but the dependence on the counter-ion valence for asymmetric systems was similar to that in systems of symmetrically charged particles [54]. The understanding of heteroaggregation processes in natural environments has been the focus of several studies. For example, Buffle et al. studied the colloidal interactions between inorganic colloids and natural organic matter (fulvic compounds as well as rigid and flexible biopolymers) to model the colloidal behaviour in natural aquatic systems. The colloidal interaction and stability depended on the size, electric charge, and conformation of the involved particles [19]. Also, Wang et al. reviewed the modelling and mechanism of heteroaggregation of nanoparticles and biocolloids (viruses, bacteria, proteins, DNA), geocolloids (clay minerals) and natural organic matter found in surface water, sediments, and soil [18].

Coupled experimental/simulation studies on heteroaggregation have been reported to gain more insight into the properties and behaviour of the resulting heteroaggregates. Cerbelaud et al. investigated the heteroaggregation of $SiO_2$ nanoparticles and $Al_2O_3$ microparticles via Brownian dynamic simulations [55]. Parameters such as Debye length and surface potential were obtained experimentally for the commercial particles and the particle-particle interactions were interpreted in terms of the DLVO theory. Both experimental and simulation studies showed that very small amounts of added $SiO_2$ can destabilize the $Al_2O_3$ suspensions by formation of aggregates, shown in Fig. 2, with good agreement between experimental and simulation results on the quantity of $SiO_2$ adsorbed on $Al_2O_3$.

Studies on heteroaggregation of different particles have also been reported in the presence of multivalent ions. Moazzami-Gudarzi et al. studied the interaction forces during homo and heteroaggregation between the oppositely charged sulfate latex and amidine latex particles in aqueous solutions containing monovalent salts or $[Fe(CN)_6]^{4-}$ anions [56]. Quantitative interpretation of the force profiles suggested the existence of DLVO type particle-particle interactions with non-DLVO short-ranged attractive components. Moreover, Cao et al. studied heteroaggregation between oppositely charged amidine and sulfate latex particles in the presence of monovalent as well as $SO_4^{2-}$, $[Fe(CN)_6]^{4-}$, and $[Fe(CN)_6]^{3-}$ multivalent ions [51]. In monovalent salt solutions, the particles are oppositely charged, while one particle type reverses its charge upon addition of multivalent ions. Trefalt et al. systematically studied the homo and heteroaggregation of carboxylate, sulfate, and amidine latex particles at different KCl and polyamines concentrations. For carboxylate latex particles, charge reversal occurred at lower concentration for polyamines with higher number of amino groups, and for heteroaggregation between sulfate and amidine latex particles, stability ratio increased with increasing KCl concentration, but the effect is less pronounced compared to that for homoaggregation [57].

The experimental conditions such as pH, ionic strength, and component concentration profoundly affect the heteroaggregation rate and the properties of the resulting heteroaggregates, and thus, considerable number of studies have explored dependence patterns. For example, Voorn et al. studied the heteroaggregation kinetics between polystyrene-*co*-poly(isobutyl methacrylate) latex spheres and γ-$Al(OH)_3$ platelets as a function of the sphere/platelet number ratio, pH, and ionic strength [58]. Mixed dispersions of relevant constituents were analyzed via time resolved dynamic light scattering. High sphere/platelet number

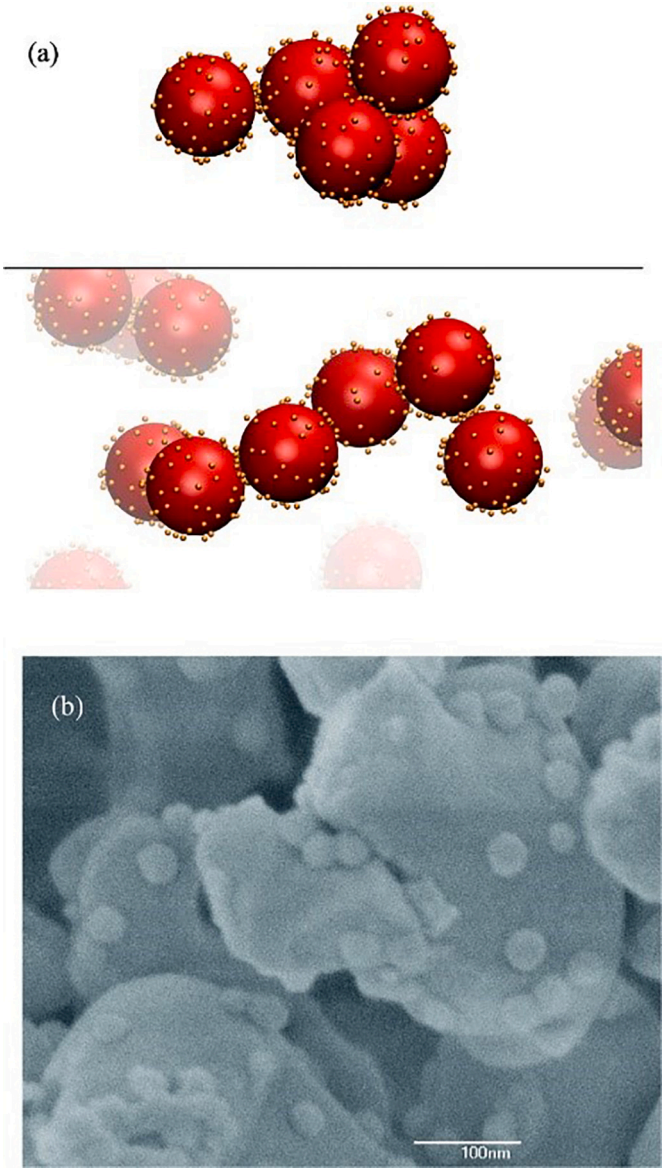


**Fig. 2.** (a) Snapshot of two agglomerates formed in the simulation and (b) Cryo-FEGSEM image of alumina particles surrounded by silica particles [55]. Reprinted (adapted) with permission from (Cerbelaud, A.;Videcoq, A.; Pagnoux, C.; Rossignol, F.; Ferrando, R., Heteroaggregation between $Al_2O_3$ submicrometer particles and $SiO_2$ nanoparticles: Experiment and simulation. *Langmuir* 2008, *24* (7), 3001–3008). Copyright (2021) American Chemical Society.

ratio should be maintained to prevent the formation of multilayer aggregates and the heteroaggregated particles were stable within a pH range of 2–9 and up to different ionic strengths depending on the aggregate size. In another study, Lin et al. measured rate constants of heteroaggregation of commercial silica as well as amidine and sulfate latex over a wide range of ionic strength and different surface charge densities. The heteroaggregation rate constants increased slowly with decreasing ionic strength, and for highly charged surfaces, the rate constant was independent of the surface charge [59].

Also, Bansal et al. used commercial negatively charged silica and positively charged alumina-coated silica particles to study heteroaggregation in aqueous dispersions by following the pH-dependent surface charging as well as heteroaggregate size, structure, and flow properties [60]. Different phases formed upon mixing the oppositely charged particles with different positive particle ratio, such new phases

ranged from gel-like at high particle ratio, while clear, turbid, and sediment (with turbid and clear supernatant) phases formed at low particle ratio.

Parsai and Kumar probed the heteroaggregation of commercial ZnO and CuO nanoparticles in aqueous dispersions at different pH, ionic strength, and nanoparticle concentration by developing empirical equations to predict the difference in zeta potential as well as their aggregation and settling rate constants. The attractive van der Waals forces dominated in aggregation, and the nanoparticle concentration was found to be the major factor affecting settling rate constant, whereas the pH and ionic strength, and nanoparticle type affected the aggregation rate constant [61].

Nakamura et al. studied the interactions between a number of negatively charged PS with silica particles in the presence of the cationic surfactant cetylpyridinium chloride [62]. PS particles were either obtained commercially or synthesized by emulsifier-free polymerization, whereas silica particles were obtained from commercial sources. The negative charge on PS and silica particles decreased as more surfactant molecules were electrostatically adsorbed onto the particles, which became positively charged when surfactant concentration exceeded the isoelectric point (IEP). In the intermediate concentration regime, both particles were oppositely charged, and clustering of different particles was enabled. By selecting the proper surfactant dose, it is possible to dictate colloidal behaviour and the associations of different particles into heterogeneous colloidal clusters.

Lu et al. studied the interaction of aqueous graphene oxide (GO) colloidal particles with three clay particles under different solution chemistry conditions [63]. Both the GO and the three clay materials were obtained commercially. A solid sample of the relevant clay mineral was added to a dispersion of GO, and the mixture was shaken for a prolonged period of time. The affinity of clay particles towards GO was in the order of montmorillonite > kaolinite > diatomite under the same experimental conditions. Increasing the ionic strength or decreasing the pH improved the immobilization of GO nanoparticles onto clay minerals due to electrostatic interactions, while the addition of tartaric acid largely prevented the heteroaggregation of GO and the mineral particles.

Assembly of different particles has also been utilized to prepare thin films. Novel thin-film freeze-drying SEM was utilized by Harley et al. to study the heteroaggregation of oppositely charged amidine and smaller sulfate PS particles at different ionic strength conditions and in the presence and absence of pre-adsorbed layers of poly(vinyl alcohol-*co*-vinyl acetate) on both particles. The presence of the polymer affected the amount of immobilized sulfate latex particles, when electrolyte concentration exceeds a critical value, which indicates that the long-range interactions between the particles largely affected the heteroaggregation rate coefficient as well as the final amount of immobilized particles [64]. Fig. 3 shows the amidine-sulfate latex hybrid particles.

Heteroaggregation rates were measured even though it occurs simultaneously with homoaggregation. Yu and Borkovec studied the heteroaggregation of positively charged amidine and negatively charged sulfate PS by mixing appropriate concentrations in KCl solutions [15]. Absolute heteroaggregation rate constants between the two particles were determined with great accuracy. Both static and dynamic light scattering were used although the latter technique was more accurate and more sensitive. In another study from the same group, Yu et al. studied heteroaggregation kinetics of commercial amidine latex and carboxyl or sulfate latex particles and pointed out that the experimental conditions can be adjusted to exclude any significant homoaggregation [65]. By mixing appropriate volumes of the relevant dispersions, apparent aggregation rate constants were determined. The rate obtained from static light scattering measurements strongly decreased with increasing scattering angle, while rates from dynamic light scattering experiments showed more complex dependence, with values found within experimental error with both techniques. A formula was proposed to estimate the hydrodynamic radius of the asymmetric particle doublet agreed well with experimental data and theoretical predictions.

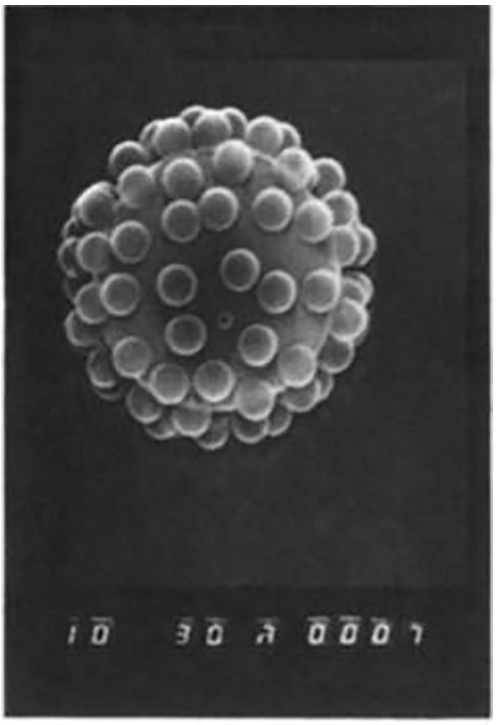

**Fig. 3.** Thin-film freeze-drying SEM image of amidine-sulfate latex hybrid [64]. Reprinted from (The adsorption of small particles onto larger particles of opposite charge. Direct electron microscope studies, 62 (1–2), Harley, S.; Thompson, D. W.; Vincent, B., *Colloids and Surfaces,* 1992, 163–176). Copyright (2021), with permission from Elsevier.

Aquatic systems such as sea and river water sources are colloidal in nature, and thus the heteroaggregation among the different particles in such systems was studied. Luo et al. investigated the heteroaggregation between positively charged $CeO_2$ and negatively charged $TiO_2$ nanoparticles in laboratory and natural water (rivers and reservoirs) [47]. In both water sources, the stability of the system generally increased with increasing $CeO_2/TiO_2$ ratio. At the same $CeO_2/TiO_2$ ratio, however, NaCl lowered the stability relative to a control sample by charge screening, while humic acid significantly increased the stability relative to the control sample by adsorbing onto the particles and preventing their approach due to steric hindrance. Fig. 4 illustrates the proposed mechanism for the competitive adsorption of humic acid onto $CeO_2$ and $TiO_2$ nanoparticles.

Also, Oriekhova and Stoll explored the heteroaggregation of positively charged polystyrene nanoplastics with negatively charged $\alpha$-$Fe_2O_3$ and alginate particles by systematic mixing of their aqueous dispersions. The three materials were obtained commercially. Polystyrene nanoplastics were found to undergo heteroaggregation with $\alpha$-$Fe_2O_3$ and alginate leading to charge neutralization and charge reversal. At 40 ppm nanoplastics, the IEP for nanoplastics-alginate occurred at 1 ppm, whereas in the nanoplastics-$\alpha$-$Fe_2O_3$ system, it occurred at 3 ppm nanoplastics dose, when the $\alpha$-$Fe_2O_3$ concentration was fixed at 5 ppm. In the triple system of nanoplastics-alginate-$\alpha$-$Fe_2O_3$, the presence of alginate led to a delay in the heteroaggregation due to a competitive interaction of alginate and $\alpha$-$Fe_2O_3$ with nanoplastics particles. Also, when dispersed in Rhône river, polystyrene nanoplastics rapidly changed their surface charge from positive to negative possibly due to the adsorption of naturally existing components such as organic matter as well as inorganic and organic polyions [23].

Moreover, the environmental impact and the fate of nanoplastics particles in aquatic systems have been explored. For example, Singh et al. investigated the aggregation and stability of polystyrene

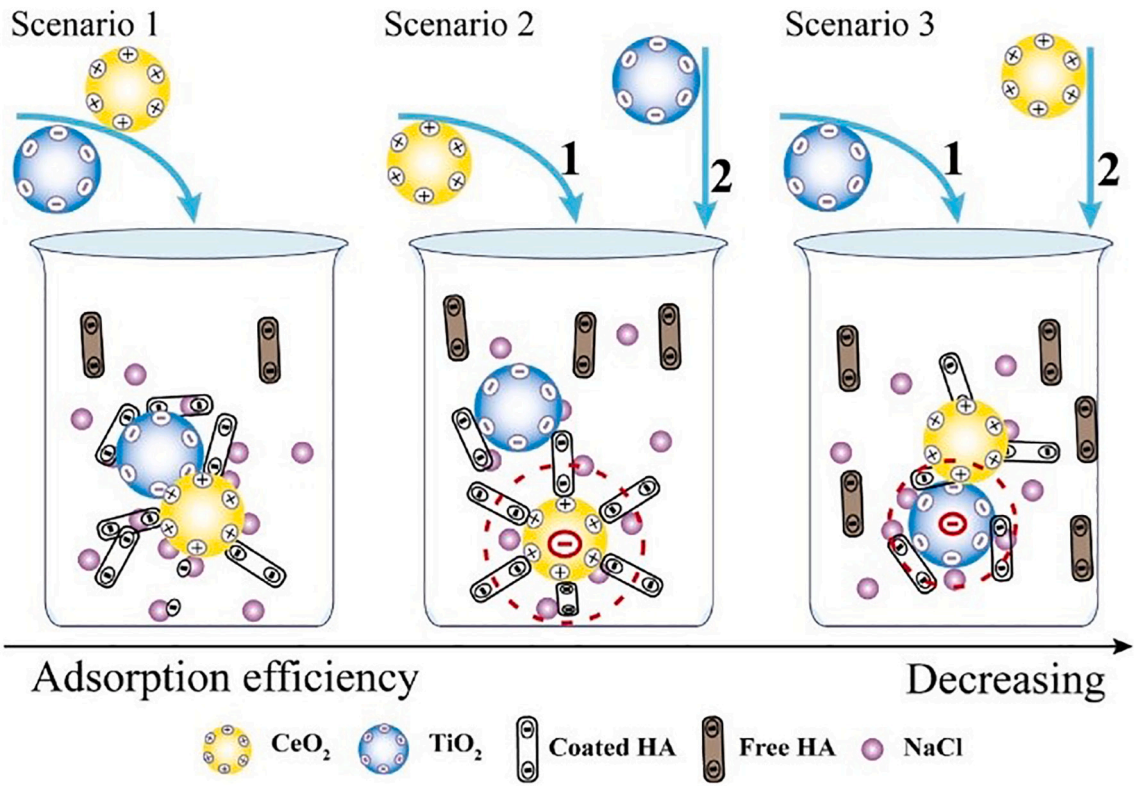


**Fig. 4.** Proposed mechanisms for the competitive adsorption of humic acid (HA) onto $CeO_2$ and $TiO_2$ nanoparticles [47]. Reprinted from (Heteroaggregation of $CeO_2$ and $TiO_2$ engineered nanoparticles in the aqueous phase: Application of turbiscan stability index and fluorescence excitation-emission matrix (EEM) spectra, 533, Luo, M. X.; Qi, X. J.; Ren, T. X.; Huang, Y. X.; Keller, A. A.; Wang, H. T.; Wu, B. R.; Jin, H. P.; Li, F. T., *Colloids Surf. A: Physicochem. Eng. Aspects,* 2017, 9–19). Copyright (2021), with permission from Elsevier.

nanoplastics in different aqueous environments (river water, seawater, and groundwater) under different ionic strengths and temperatures, and in the presence of dissolved organic matter (humic acid), inorganic soil colloids (bentonite clay particles), and heavy metal salts ($ZnCl_2$, $CdCl_2$, and $HgCl_2$). Lower critical coagulation concentration (CCC) values were obtained at higher temperature and in the presence of multivalent ions, whereas humic acid stabilized nanoplastics due to steric repulsion. The highest rate of aggregation was observed in seawater followed by river water and ground water, which can be attributed to the complex chemistry of these systems [66].

The aggregation tendency of particulate organic matter (POM) in soil was investigated to probe its effect on the performance of nanoparticles in remediation technologies. Wang et al. investigated the effect of POM on the potential of the Se nanoparticles (Se NPs) to capture toxic $Hg^0$ in soil solution. The POM was extracted from black soil, while Se NPs were produced by reduction of $Na_2SeO_3$ using the selenite-reducing bacterium *Citrobacter freundii Y9*. The soil solution was prepared by mixing black soil with Milli-Q water and the centrifuged supernatant was filtered and purified by dialysis. Low concentrations of POM (0–80 mg/L) inhibited heteroaggregation with Se NPs and led to enhanced stability of Se NPs, while POM particles underwent homoaggregation at higher POM concentration (80–100 mg/L). At neither concentration range was the Se NPs removal ability of $Hg^0$ affected in the presence of POM [52].

Barton et al. assessed the relative affinity of several nanoparticles to undergo heteroaggregation with larger particles in activated sludge [67]. The relative affinity was found to be in the order of pristine $CeO_2$ NPs, $TiO_2$ NPs, ZnO NPs > poly(vinyl pyrrolidone) (PVP)-modified Ag NPs > citrate- functionalized $CeO_2$ NPs > gum Arabic-modified Ag NPs. The trends in the removal of solids from sludge were similar to those of the affinity, indicating that higher affinity leads to more effective removal by the nanoparticles.

### 2.2. Sphere-plate systems

Tombácz et al. probed the heteroaggregation of magnetite ($Fe_3O_4$) nanoparticles, obtained by co-precipitation, with commercial sodium montmorillonite [68]. Fractal aggregates formed due to Coulombic interactions in suspensions of either particles as well as mixed suspensions. Potentiometric acid-base titration indicated that magnetite-montmorillonite hybrids occurred at low ionic strength and only in acidic pH conditions when the amphoteric sites develop a positive charge.

Guo et al. investigated the charge-dependent interactions of commercial $CeO_2$ nanoparticles (NPs) with kaolinite via HRTEM and atomic force microscopy. The $CeO_2$ NPs attached to kaolinite platelets via electrostatic interactions. The hybrid was prepared by dispersing a certain amount of kaolinite in an aqueous dispersion of $CeO_2$ NPs. Neutral and positively charged $CeO_2$ NPs showed a strong affinity to kaolinite surfaces, whereas negatively charged $CeO_2$ NPs exhibited weak attachment to kaolinite. Such change in surface charge density in kaolinite might adversely affect the bioavailability of nutrients to plants, because of the interactions of kaolinite with its surrounding in soil pore water [69].

The heteroaggregation of three types of particulate zero-valence iron nanoparticles (nZVI) and two types of clay mineral particles (CMP) (kaolinite and montmorillonite) was studied by Wang et al. at different pHs (at 3.5, 6.5 and 9.5) and various nZVI-to-CMP mass ratios. Aqueous dispersions of the commercially obtained nZVI and CMP were mixed in the desired ratio. The pH was found to affect the dominant forces responsible for the formation of nZVI-CMP. Lewis acid-base (AB) interactions predominated in neutral or alkaline conditions, while electrostatic interactions dominated under acidic conditions. Both AB and van der Waals interactions could enhance the formation of nZVI-CMP heteroaggregates under neutral or alkaline conditions to overcome

electrostatic repulsion. The interaction behaviour of nZVIs with CMP might be extended to understand the interaction of nZVI with biocolloids such as proteins, DNA, viruses, and bacteria, where AB interactions are significant [44].

### 2.3. Miscellaneous systems

Khalil et al. utilized heteroaggregation to prepare thin films of nanofibrillated cellulose (NFC) and Ag NPs [70]. Both cellulose and Ag NPs were prepared and further coated with PVP as a stabilizing agent. The NFC-AgNPs composite was prepared by mixing aqueous suspensions of cellulose and AgNPs and subsequent homogenization. The NFC/PVP/AgNPs composite was used as a film material, which was prepared by introducing the composite suspension into Petri dishes followed by prolonged drying at elevated temperatures. The homogenous nanocomposite showed promising electrical conductivity and high tensile strength, a potential antistatic and static dissipative materials. The NFC/PVP/AgNPs mass ratio of 25/75/2 showed the highest electrical conductivity, which ranged from $2.36 \times 10^{-10}$ S/cm to $1.5 \times 10^{-6}$ S/cm at 30 °C.

In another study, Hassan et al. probed the effect of the addition of barium titanate (BT) nanoparticles into cellulose nanofibers (CNF) on the physicochemical properties of CNF/BT composite thin films [71]. The oxidized nanofibers were produced from bleached bagasse pulp, while BT nanoparticles were prepared from barium carbonate and titania. The nanocomposite was prepared by mixing the aqueous suspensions of CNF and BT at different mass ratios in a Teflon Petri dish along with a fixed ratio of glycerol. The resulting composites showed homogenous distribution of BT in the CNF matrix as well as good thermal stability. Also, the incorporation of BT nanoparticles to CNF decreased the tensile strength of the films but it increased the dielectric constant of the nanocomposites up to 5% (w/w) BT. In addition, the values of activation energy decreased as the doping level of BT nanoparticles increased, which indicates that the conductivity has an electronic and ionic nature.

Huynh et al. probed the effects of humic acid and the mass ratio of negatively charged multi-walled carbon nanotubes (CNTs) and positively charged hematite nanoparticles on their heteroaggregation rates. Hematite nanoparticles were prepared by forced hydrolysis [72]. Certain volumes of hematite and CNTs dispersions were mixed at the required CNTs/hematite ratio. By altering the mass ratio, the heteroaggregation rates and information on the mechanism were obtained. At the optimal ratio, heteroaggregation rate was three times faster than the one measured for homoaggregation of hematite. Higher ratios caused a significant decrease in the heteroaggregation rate and the addition of humic acid had no effect on the tendencies in the heteroaggregation rates, but it reduced the maximum aggregate growth rate. Fig. 5 shows cryo-TEM images of CNT/hematite heteroaggregates at different ratios.

Jurado and Galvez used ex situ and in situ heteroaggregation to prepare organic-inorganic systems based on amyloid fibrils of both apoferritin (APO) and β-lactoglobulin (BLG), and inorganic nanoparticles [73]. Gold nanospheres (AuNSs) were obtained commercially while, maghemite and gold nanorods (AuNRs) were prepared by coprecipitation and seed-mediated growth method, respectively. The ex situ heteroaggregation was achieved by mixing aqueous suspensions of either APO or BLG amyloid fibrils with those of AuNs, AuNRs or maghemite and the resulting suspensions were then incubated for a prolonged period of time. The systems of APO fibrils with AuNRs, AuNSs, and PdNPs were also prepared in situ by preparing the relevant particles in the presence of APO fibrils. For the former approach, the assemblies showed improvement in magnetic anisotropy, probably due to fibril organisation and dipole-dipole interactions. For such organic-inorganic systems, the physical properties can be tuned by altering the nanoparticle composition, size, and shape while elastic and mechanical properties can be adjusted by altering the biological templates.

Liu et al. used GO, prepared by Hummer's method, to synthesize GO-$Al_2O_3$ hybrid in attempt to accurately understand the fate of the GO in the environment as well as the effect of GO size on its homo and heteroaggregation behaviour [74]. Aqueous dispersions of differently sized GO sheets were mixed with those of commercial $Al_2O_3$ particles at different pH and ionic strength conditions. The heteroaggregation of GO-$Al_2O_3$ hybrid was attributed to the electrostatic attraction and

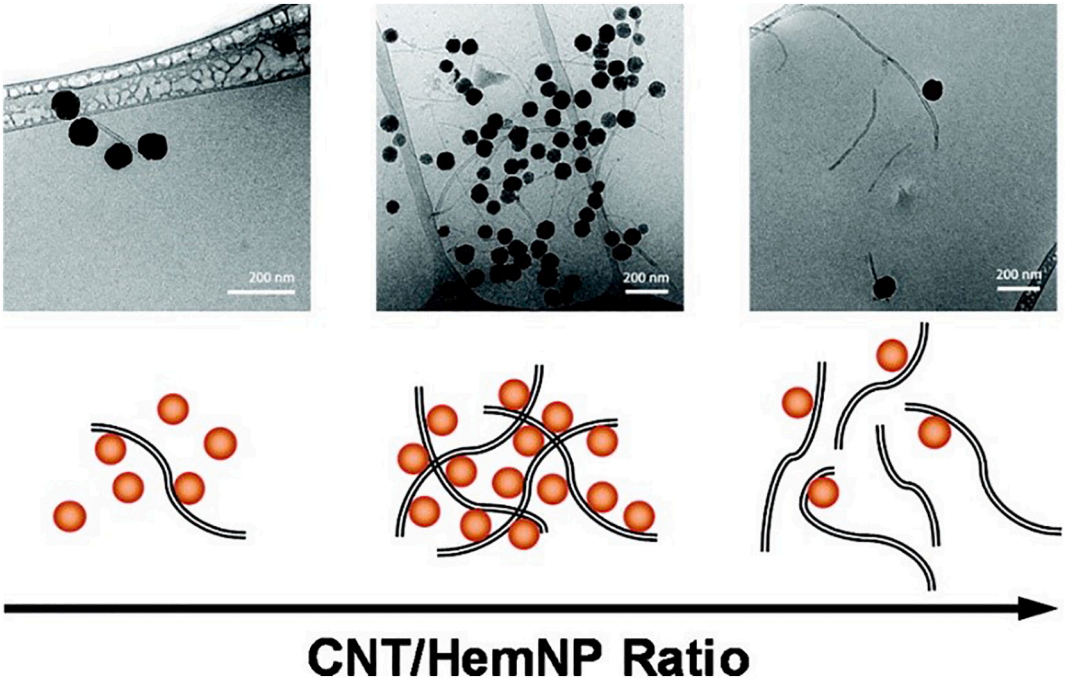


**Fig. 5.** Representative cryo-TEM images of heteroaggregates of CNT and hematite (HemNP) at (upper left) low, (upper center) optimal and (upper right) high CNT/HemNP ratios. Proposed heteroaggregation mechanisms at different nanoparticle distributions are shown at the bottom [72]. Reprinted (adapted) with permission from (Huynh, K. A.; McCaffery, J. M.; Chen, K. L., Heteroaggregation of multiwalled carbon nanotubes and hematite nanoparticles: rates and mechanisms. *Environ. Sci. Technol.* 2012, *46* (11), 5912–5920). Copyright (2021) American Chemical Society.

hydrogen bonding in aqueous media. The attachment capacity of large GO sheets onto $Al_2O_3$ particles was greater than that of small GO, and the effect of the pH on the adsorption of $Al_2O_3$ was different for different GO. The increase in the ionic strength facilitated the heteroaggregation between GO and $Al_2O_3$.

Besides, the effects of minerals on the adsorption process helps understand the fate of contaminants in natural water environments. For example, Jiang et al. found that the negatively charged $SiO_2$ and positively charged $Al_2O_3$ NPs largely prevented the adsorption of 17β-estradiol onto GO and prolonged the adsorption equilibration time [45]. The oxide NPs were obtained commercially, while GO was prepared using the modified Hummers' method. Various amounts of NPs were added into a series of pre-dispersed GO suspensions, and the homogenized NPs-GO suspensions were then mixed with 17β-estradiol solutions. The inhibition was more pronounced in the case of $Al_2O_3$ than $SiO_2$ due to the electrostatic attraction, which led to heteroaggregation between the oppositely charged $Al_2O_3$ and GO lamellae. Moreover, GO tended to first homoaggregate and then heteroaggregate with $SiO_2$, as revealed by DLVO calculations.

Also, Chen et al. investigated the influence of particle size of minerals on the adsorption of pollutants such as sulfamethoxazole on multi-walled CNT in natural water in the presence of $SiO_2$ or $Al_2O_3$ nanoparticles of different sizes [75]. Both $SiO_2$ and $Al_2O_3$ inhibited the sulfamethoxazole adsorption on CNTs by competitive heteroaggregation of the latter with either nanoparticles. The extent of inhibition depended on the size and type of nanoparticles. The amount of sulfamethoxazole adsorbed on CNTs decreased with increasing $SiO_2$ particle size but increased with increasing $Al_2O_3$ particle size due to the different heteroaggregation patterns with CNTs. Electrostatic attraction between the oppositely charged CNTs and $Al_2O_3$ favoured their heteroaggregation, while repulsive interactions between CNTs and $SiO_2$ increased with increasing $SiO_2$ particle size. Fig. 6 shows TEM images of CNT-nanoparticle composite of different particle size.

### 2.4. Conclusive remarks

As shown above, the introduction of inorganic nanostructured materials in aqueous media brings about different regimes of interactions not only among similar and dissimilar particles, but also between particles and the dispersion medium. The collective outcome of these interactions is the generation of surface charge responsible for the stability of colloidal systems of single-component composition. The nature and magnitude of the surface charge depend on the intrinsic properties of the material as well as the experimental conditions such as the pH and ionic strength. The DLVO theory emphasizes that the overall stability of such colloidal systems of particles in aqueous dispersions is dependent on the contribution of two major forces, attractive van der Waals and repulsive electrostatic forces. Conditions such as high ionic strength, low dielectric solvents, and pH near the isoelectric point significantly weaken the electrostatic repulsion, resulting in domination of van der Waals forces and subsequent aggregation. Moreover, the presence of oppositely charged particles spark the existence of non-DLVO type electrostatic attractive force that leads to heteroaggregation. Such observation presents a mechanism to deliberately and controllably trigger particle-particle heteroaggregation via manipulation of experimental conditions such as pH or surface functionalization with charged polyelectrolytes that cause particles to be oppositely charged. Heteroaggregation could also arise due to chemical interactions such as Lewis acid-base interactions as the case with nZVI and clay mineral particles and also via hydrogen bonding, when nanoparticles with abundant oxygen-containing groups are present, as we have seen with GO and $Al_2O_3$. In the following chapters, the implementation of these

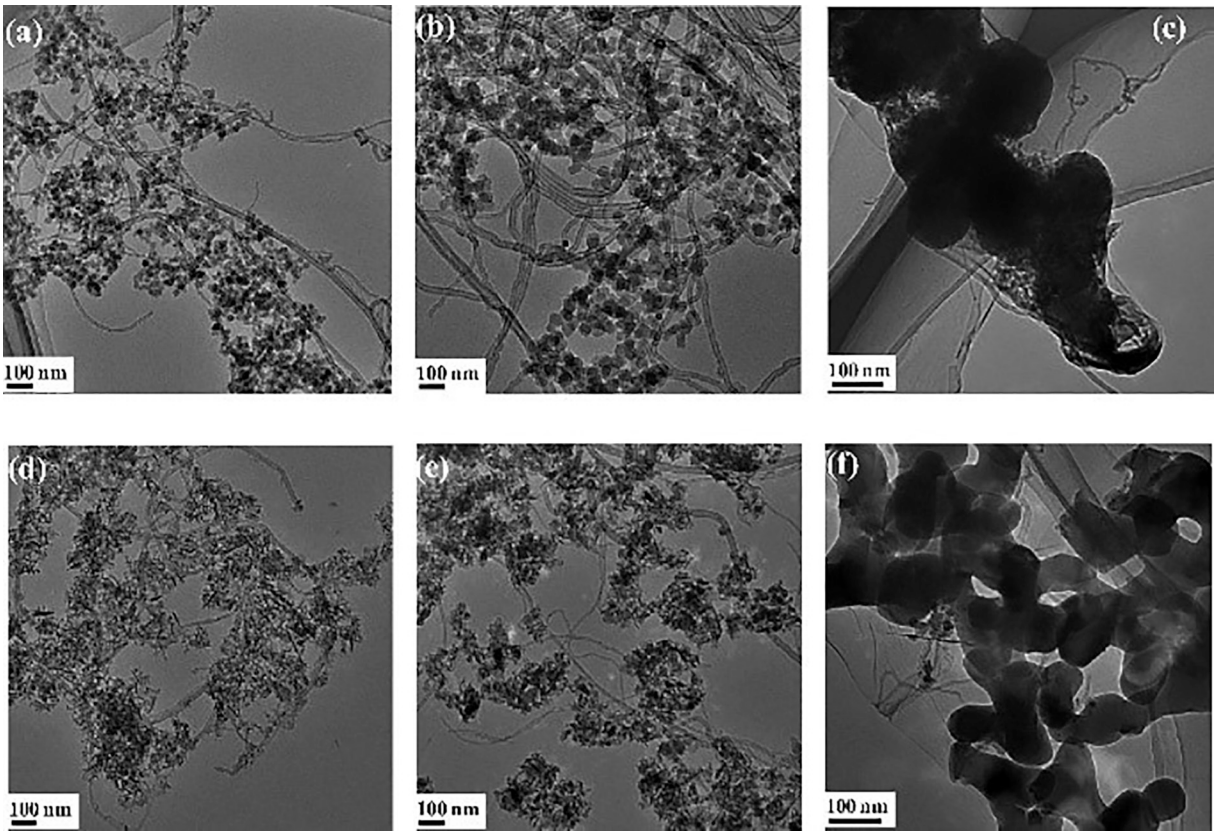


**Fig. 6.** TEM images of (a, b, c) CNTs- $SiO_2$ and (d, e, f) CNTs-$Al_2O_3$ composites ((a, b, c): 15 nm, 30 nm, and 100 nm $SiO_2$, (d, e, f): 20 nm, 50 nm, and 100 nm $Al_2O_3$, respectively) [75]. Reprinted from (Size-dependent impact of inorganic nanoparticles on sulfamethoxazole adsorption by carbon nanotubes, 316, Chen, B.; Sun, W. L.; Wang, C. H.; Guo, X. Y., *Chem. Eng. J.* 2017, 160–170). Copyright (2021), with permission from Elsevier.

heteroaggregation principles to fabricate novel and/or functional hybrid materials with promising physicochemical features in numerous applications is reviewed.

## 3. Novel heterostructures: heteroaggregation and characterization

In this section, various heterostructures of novel physicochemical features are discussed. They were prepared by heteroaggregation of particle dispersions and the observed new phenomenon is foreseen to be utilized in some fields, i.e., significant effort was made on structural characterization, however, applications only proposed based on the determined properties. We consider sphere-sphere, plate-plate, and sphere-plate geometries.

### 3.1. Sphere-sphere systems

The photocatalytic potential of heteroaggregated structures of $SnO_2$ and $TiO_2$ particles has been explored by de Mendonça et al., who prepared $TiO_2$-$SnO_2$ structures with semiconductor surface by microwave-assisted heteroaggregation of dispersions of $TiO_2$ and $SnO_2$ nanoparticles [76]. $TiO_2$ nanoparticles were synthesized by the decomposition of a peroxotitanium complex under hydrothermal conditions, while $SnO_2$ nanoparticles were obtained by hydrolysis. The $TiO_2$-$SnO_2$ heterostructures were formed by mixing a $TiO_2$ dispersion of fixed concentration with differently concentrated $SnO_2$ dispersions followed by hydrothermal treatment at varying time and temperature in a microwave oven. The photocatalytic properties of $TiO_2$-$SnO_2$ were attributed to the heterojunctions that were formed during the treatment step. When irradiated by UV light, $TiO_2$-$SnO_2$ generates surface hydroxyl radicals that react with and transform terephthalic acid to a fluorescent product.

Siedl et al. explored the charge transfer processes in $TiO_2$-$SnO_2$ hybrid by monitoring the changes in surface charge as well as its effect on the aggregation behaviour and photo-induced charge separation [29]. $TiO_2$ and $SnO_2$ nanoparticles were obtained by metal organic chemical vapor synthesis, and the $TiO_2$-$SnO_2$ hybrid was formed by dispersing certain amounts of the nanoparticles in a solution of formic acid, that serves to adjust the surface charge on particles, followed by annealing at high temperature. The adjustment of surface charge and annealing enabled the formation of a blended hybrid that possesses high heterojunction concentration and exhibits enhanced cross section for charge separation due to effective interfacial charge transfer across the particle-particle interfaces. These interfacial phenomena make such hybrid systems excellent candidates for such applications as photocatalysis, water splitting, and solar energy conversion.

The effect of reaction conditions on the structural properties of gel network was evaluated by Martínez-Pedrero et al. via heteroaggregation of latex and carbon black particles. The gel was prepared by mixing particles of surfactant-functionalized carbon black and natural rubber latex, where the SDS surfactant served as a stabilizing surfactant that tunes the interaction between the two particles [11]. The gel elasticity was tuned by changing the concentration of SDS, ranging from a reversible weak gel state to an irreversible elastic solid state.

Dušak et al. showed that the nature of interaction forces responsible for the formation of heteroaggregates profoundly affects their properties. Spherical carboxyl-functionalized and silica-coated maghemite nanoparticles were heteroaggregated with larger amino-functionalized silica spherical nanoparticles [50]. Silica NPs were synthesized using a modified Stöber process, while its amino functionalization was achieved by grafting. On the other hand, maghemite was synthesized by the *co*-precipitation method and silica coating was carried out using the hydrolysis and polycondensation of tetraethoxysilane, while carboxyl coating was performed with covalent grafting. The electrostatically driven heteroaggregation was achieved by vigorous mixing of aqueous suspensions of silica and maghemite. The uniformity of the surface coverage of maghemite depended on the type of interparticle interactions involved, chemical interactions resulted in more homogenous and greater coverage compared to electrostatic interaction. Fig. 7 shows TEM images of heteroaggregates at different conditions.

The aggregation pattern of metal oxides was found to depend on the pH conditions, Yi et al. used commercial $CeO_2$ nanoparticles with pyrogenic carbonaceous material (PCM) NPs to probe the effect of the pH on heteroaggregation behaviour by mixing the corresponding aqueous dispersions at the desired ratio and observing the changes in hydrodynamic radius and zeta potential [77]. At pH 5.3, heteroaggregation is favourable only at appropriate experimental conditions leading to charge neutralization and charge reversal, where repulsive electrostatic forces dominate at high and low PCM concentrations, whereas unstable systems were obtained at intermediate PCM concentrations. Around pH 7.1, $CeO_2$ particles are neutral and form unstable dispersion, while PCM is negatively charged and forms stable dispersions. Heteroaggregation occurred by charge-accumulation and core-shell stabilization mechanism, where PCM binds to and forms a negatively charged shell on the neutral surface of $CeO_2$ core.

Heteroaggregation of spherical particles of similar chemical composition, but with a significant difference in particle size has been reported by Zanini et al., who prepared heterostructures with various surface roughness of oppositely charged and differently sized silica particles, as shown in Fig. 8. The positive charge on smaller silica particles was achieved by surface functionalization with PDADMAC polyelectrolyte. Additionally, the heteroaggregation of PNIPAM-based microgels onto commercial PS microbeads was attributed to hydrophobic interactions. The size of adsorbed microgels changed with the pH conditions and the surface coverage of microgels was higher in acidic conditions [78].

### 3.2. Sphere-plate systems

Veschambres et al. prepared nanocomposite films of particles of layered double hydroxides (LDH) and latex by heteroaggregation and solvent casting process [79]. The latex was synthesized by surfactant-free polymerization of methyl methacrylate (MMA) monomers and butyl acrylate (BA) co-monomers. MgAl-$CO_3$-LDH, on the other hand, was prepared by flash co-precipitation followed by hydrothermal treatment. The electrostatic interactions led to the heteroaggregation between the oppositely charged LDH and latex particles upon mixing the corresponding dispersions, the formed LDH-latex hybrid was then transferred into a special chamber to form LDH-latex films. The microstructure could be controlled by varying the size of the latex beads and the LDH layers. Fig. 9 shows low and high magnification TEM images of composites at different LDH contents. The films showed a homogeneous cellular network of LDH layers, with higher LDH content resulting higher wall thickness. At high temperatures, the network is stiff enough to induce a mechanical percolation in the composites, when pure matrix shows a viscous behaviour.

Ji et al. prepared a porous nanomaterial by heteroaggregation between hematite and montmorillonite particles over a pH range of 2.5–7.5, under which they possess positive and negative charge, respectively [80]. Hematite was synthesized by forced hydrolysis while montmorillonite was obtained commercially. Dispersions of both particles were slowly mixed under intensive agitation, and the aggregate formation was monitored by turbidimetric titration, which showed that particle aggregate formation depends on the concentration of the particles added initially to the dispersions. Fig. 10 shows the possible heterostructures of montmorillonite sheets with differently sized hematite particles. The mass ratio affected the number of pores and the specific surface area of the composite. With increasing hematite content, the amount of the pores with an equivalent diameter of about 4 nm decreased, while those having a diameter of 10–20 nm increased.

Voorn et al. reported the formation of various sphere-platelet hybrids by simple mixing of aqueous dispersions of gibbsite with different silica

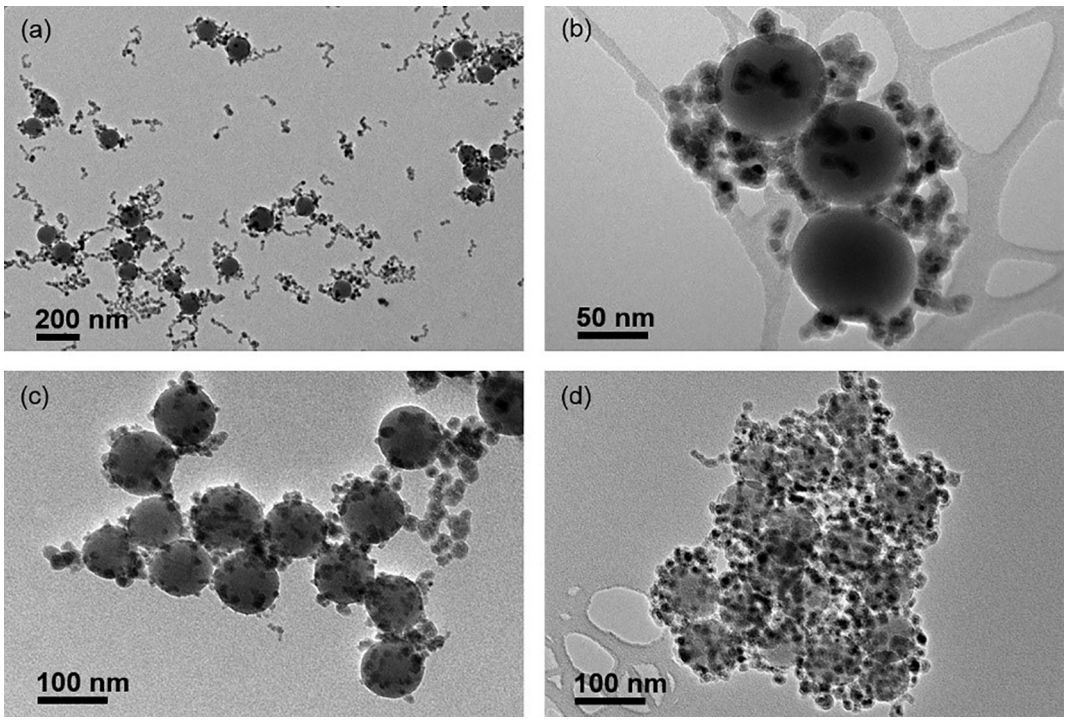


**Fig. 7.** TEM images of maghemite-silica heteroaggregates at (a, b) lower and (c) higher maghemite concentration, and at (d) lower maghemite concentration with increased ionic strength [50]. Reprinted from (Controlled heteroaggregation of two types of nanoparticles in an aqueous suspension, 438, Dusak, P.; Mertelj, A.; Kralj, S.; Makovec, D., *Journal of Colloid and Interface Science*, 2015, 235–243). Copyright (2021), with permission from Elsevier.

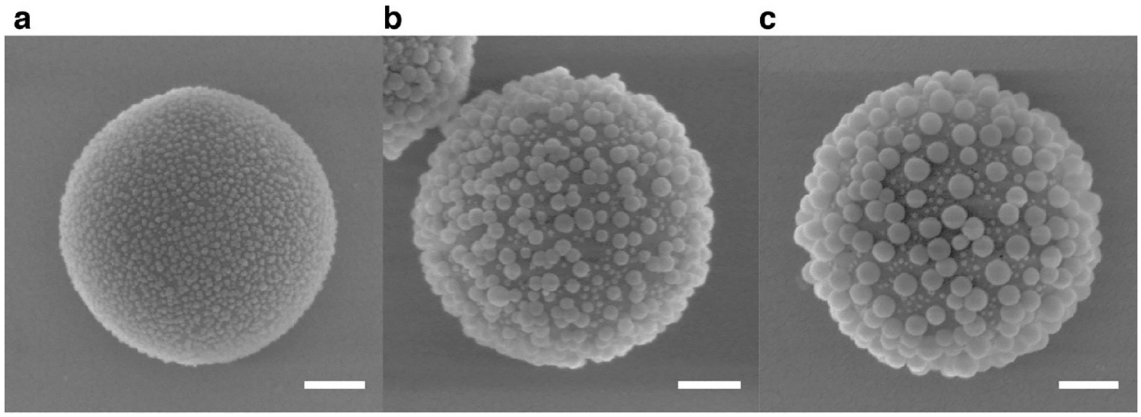


**Fig. 8.** Heterostructured silica (raspberry-like) particle. Silica particles of (a) 12 nm (b) 39 nm and 12 nm (c) and 72 nm and 12 nm silica particles adsorbed onto positively charged larger silica particles with average diameter of 1 μm. The scale bars represent 200 nm [78]. Reprinted from (Fabrication of rough colloids by heteroaggregation, 532, Zanini, M.; Hsu, C. P.; Magrini, T.; Marini, E.; Isa, L., *Colloids and Surfaces A: Physicochemical and Engineering Aspects*, 2017, 116–124). Copyright (2021), with permission from Elsevier.

and latex particles including polystyrene, poly(isobutyl methacrylate), and poly(butyl methacrylate) (PBMA) [81]. The anionic latex particles were synthesized by feed emulsion polymerization and silica particles were obtained commercially. The heteroaggregated particles were annealed above the glass transition temperature of the polymer to ensure a thin polymer layer covering the gibbsite platelets is formed. The cryo-TEM images of gibbsite-PBMA composite are shown in Fig. 11. The colloidally stable anisotropic hybrid particles possess a single layer of spheres on each side of the gibbsite platelets.

Yang et al. prepared a PS-LDH composite by heteroaggregation of the oppositely charged materials to probe the effect of different emulsifiers on the strength of interaction and polymeric properties [82]. The MgAl-LDH was prepared by the co-precipitation method, while PS was prepared by emulsion and soap-free emulsion polymerization using SDS, CTAB, and HMPS as emulsifiers. The aqueous suspension of LDHs was slowly added to the PS emulsion, and the hybrid formation was driven by the electrostatic forces between anionic polymer particles and cationic LDHs platelets. A reactive emulsifier produced a stronger interaction and higher glass transition temperatures, and well-dispersed LDHs platelets resulted in composites of improved thermal stability.

Pavlovic et al. investigated the aggregation of polymer latex particles in the presence of LDH platelets of different compositions [83]. The MgAl-$CO_3$-LDH and MgAl-$NO_3$-LDH platelets were synthesized by flash co-precipitation followed by hydrothermal treatment, while P(MMA-*co*-BA) latex particles were prepared by surfactant-free emulsion polymerization. The oppositely charged species form the LDH-P(MMA-*co*-BA) hybrid upon mixing their aqueous dispersions due to the electrostatic attraction. Fig. 12 shows a schematic representation of the

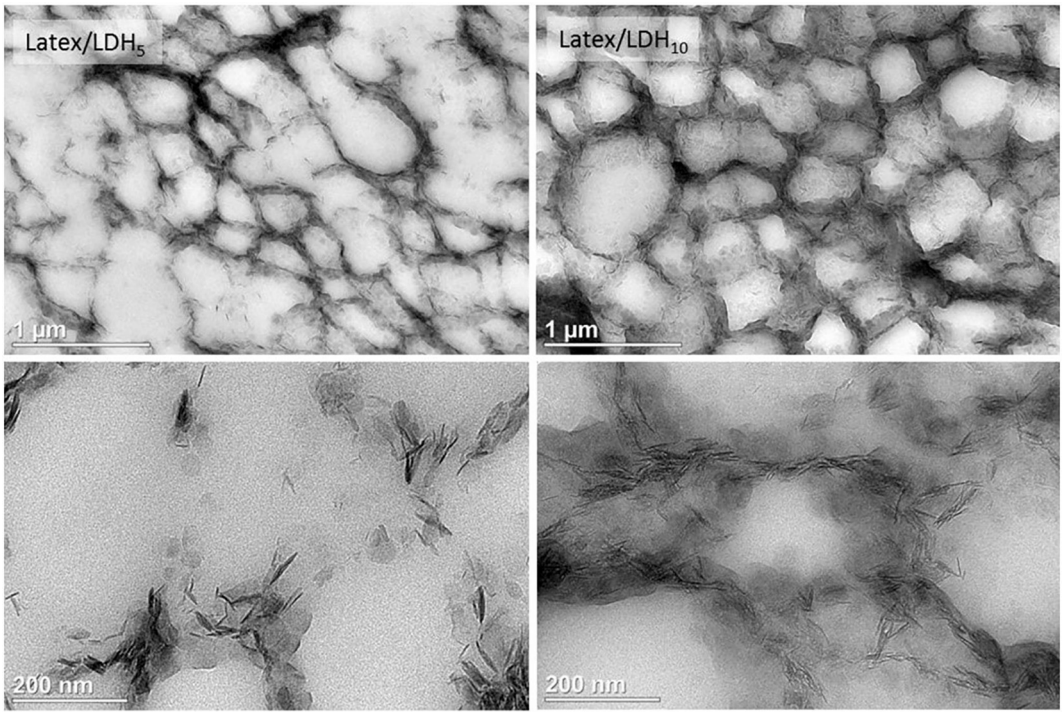


**Fig. 9.** TEM images of Latex/$LDH_5$ and Latex/$LDH_{10}$ samples (the subscript indicates the volume content of the LDH) at different magnifications [79]. The formed LDH network is well-visible on the pictures. Reprinted from (Layered double hydroxides: Efficient fillers for waterborne nanocomposite films, 130, Veschambres, C.; Halma, M.; Bourgeat-Lami, E.; Chazeau, L.; Dalmas, F.; Prevot, V., *Applied Clay Science*, 2016, 55–61). Copyright (2021), with permission from Elsevier.

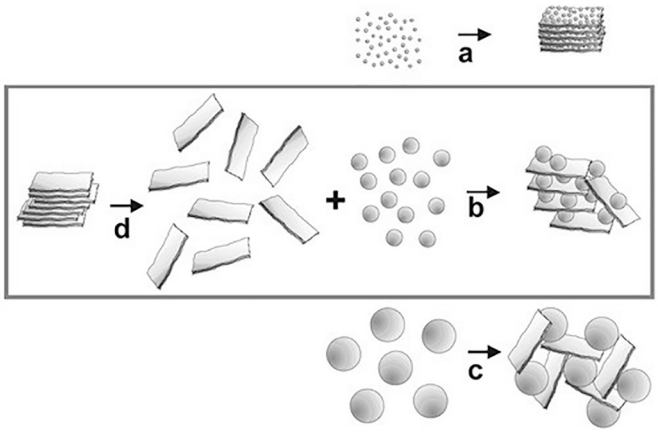


**Fig. 10.** Schematic illustration of (a) the preparation of organic-inorganic composites, (b) heteroaggregation with sol particles, and (c) emulsions, while synthesis of delaminated montmorillonite particles is shown in (d) [80]. Reprinted (adapted) with permission from (Ji, Y. Q.; Black, L.; Weidler, P. G.; Janek, M., Preparation of nanostructured materials by heterocoagulation-interaction of montmorillonite with synthetic hematite particles. *Langmuir* 2004, *20* (22), 9796–9806). Copyright (2021) American Chemical Society.

aggregation process of the P(MMA-*co*-BA) spheres with the adsorbed MgAl-$CO_3$-LDH platelets on the surface. Electrostatic attraction between LDH and latex led to charge neutralization and reversal when the LDH dose was increased. The LDH-latex particles rapidly aggregated near the IEP but formed stable suspensions at LDH doses away from IEP.

### 3.3. Plate-plate systems

Li et al. fabricated NiFe-LDH/$MnO_2$ nanocomposite via layer-by-layer self-assembly and flocculation methods [84]. The SEM and TEM images in Fig. 13 highlight the structural features of nanocomposites obtained by LBL method and flocculated methods. The $MnO_2$ nanosheets and NiFe-LDH were prepared separately via hydrothermal synthesis. For the flocculation process, the colloidal suspension of delaminated NiFe-LDH nanosheets was slowly added into the formamide suspension of $MnO_2$ nanosheets to form $Ni^{2+}$–$Fe^{3+}$ LDH/$MnO_2$ with plate-like morphology. The precipitated flocculate was dried with nitrogen gas. Layered NiFe-LDH/$MnO_2$ was also prepared by sequential adsorption procedure. Cyclic voltammetry indicated good capacitance behaviour with an initial capacitance of 104 F/g for the material obtained by the aggregation process, which makes the nanocomposite a good potential candidate for use in lithium-ion batteries and supercapacitors.

Nethravathi et al. reported the preparation of co-stacked smectite clay/GO composites through delamination and re-stacking [85]. GO was prepared by the Hummers-Offeman method and its interlayers were intercalated with octylamine (OA) in the presence of small amounts of n-hexane. Commercial bentonite clay was modified by intercalating its interlayers with cetyltrimethyl ammonium (CTA) to give smectite-CTA. The GO-smectite composites were obtained by mixing and sonicating required volumes of the respective dispersions. The final composition is not uniform and has many smectite-rich and carbon-rich regions. Also, the clay component of the composites could be removed to obtain exfoliated and porous graphite.

Lagaly et al. probed the effect of mass ratio in composites of MgAl-LDH and sodium montmorillonite clay (extracted from Wyoming bentonite) on their mechanical properties. Composites were prepared by simple mixing of the corresponding dispersions [86]. The mass ratio as well as the presence of salts largely affected the mechanical stability as well as the aggregation pattern in the system. Heteroaggregation occurred when the LDH and clay mass fractions were 0.2 and 0.06, respectively. Maxima in the yield value and storage modulus was observed when the LDH mass ratio was 0.4–0.5. When the LDH was in excess, a steep decrease was observed in both the yield value and storage modulus, indicating a deterioration in mechanical properties, which can be utilized in future applications.

Huang et al. studied the effect of kaolinite and goethite associations

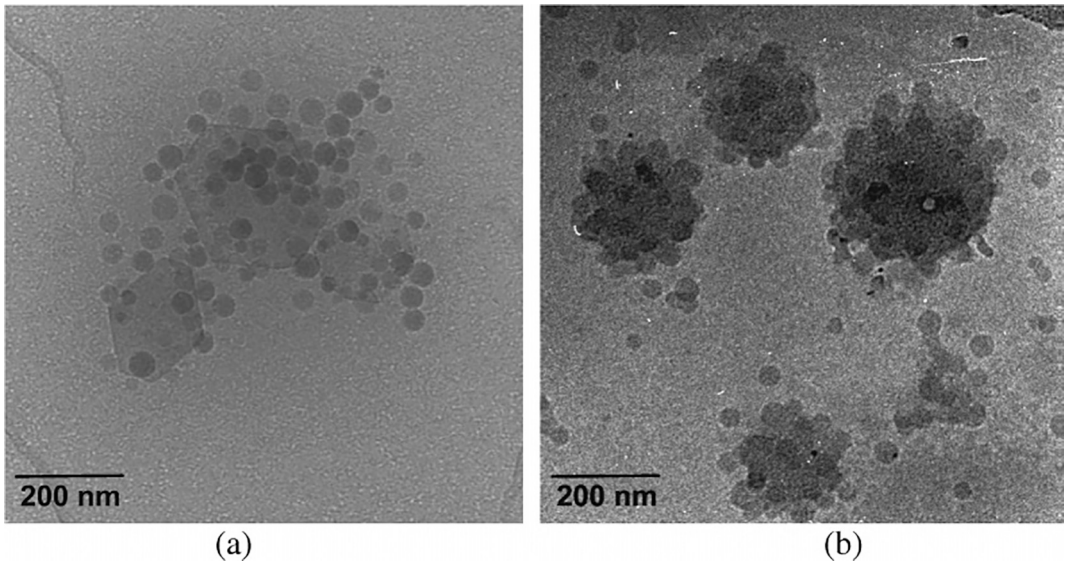


**Fig. 11.** Cryo-TEM images of cationic gibbsite with anionic PBMA particles at (a) ~0.3 mM and (b) ~0.9 mM NaCl [81]. Reprinted (adapted) with permission from (Voorn, D. J.; Ming, W.; van Herk, A. M.; Bomans, P. H. H.; Frederik, P. M.; Gasemjit, P.; Johanssmann, D., Controlled heterocoagulation of platelets and spheres. *Langmuir*, 2005, 21 (15), 6950–6956). Copyright (2021) American Chemical Society.

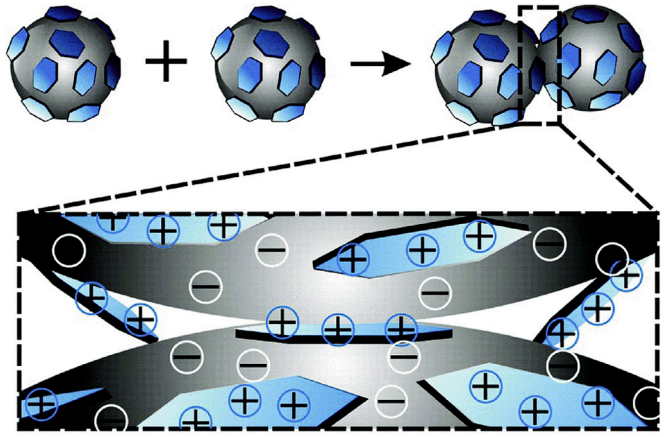

**Fig. 12.** Schematic representation of the aggregation process of the P(MMA-*co*-BA) spheres with the adsorbed MgAl-$CO_3$ platelets on the surface [83]. Reproduced from (Pavlovic, M.; Rouster, P.; Bourgeat-Lami, E.; Prevot, V.; Szilagyi, I., Design of latex-layered double hydroxide composites by tuning the aggregation in suspensions. *Soft Matter*, 2017, 13 (4), 842–851) with permission from The Royal Society of Chemistry.

(KGA) on the stability of GO in aquatic systems under different pH and ionic strength conditions as well as various GO concentrations by systematic introduction of clay minerals in GO dispersions [87]. The GO was prepared via improved Hummer's method. Heteroaggregation occurred when the pH was lower than 6 or 5, depending on the clay, and decreased with increasing GO concentration. The CCC of GO in the presence of KGA containing 10% goethite increased from less than 1 mM NaCl to 5 mM NaCl with the increase of pH from 5.5 to 9.

### 3.4. Miscellaneous systems

Heteroaggregation has been used to adsorb polysaccharide particles on fibrils. Jones et al. reported the formation of fibrils-polysaccharide complex by titrating β-lactoglobulin fibrils with the oppositely charged κ-carrageenan polysaccharide particles at low pH [88], which enabled studying the obtained morphology and mechanism of complex formation. The fibrils of β-lactoglobulin are formed by heating the β-lactoglobulin at low pH. The formation of aggregates occurred when the polysaccharide particles were attached along the protein fibrils. The attachment efficiency increased with the increase in the κ-carrageenan concentration, with maximum complexation efficiency occurred at a protein-to-polysaccharide weight ratio of 5:3. Fig. 14 shows a graphical representation of the fibrils-polysaccharide complex prepared by the heteroaggregation process.

CdSe-silica/Au nanowires and Au-silica/Au nanowires with drug delivery potential were reported by Pita et al. [89]. Au nanowires, prepared by soft solution phase synthesis, were coated with ultrathin silica layer via Stöber method. Then, differently sized nanoparticles of CdSe and Au were prepared and separately dispersed in toluene. The CdSe-silica/Au nanowires and Au-silica/Au nanowires, shown in Fig. 15, were prepared by mixing and subsequent sonicating of dispersion of silica/Au nanowires with the relevant dispersion of either CdSe or Au nanoparticles. The total coverage of Au nanowires increased with the particle size due to the presence of attractive van der Waals forces. Analysis of the recorded Raman peaks for bare and incorporated CdSe showed higher intensity for the latter owing to the generated surface plasmon propagation, which makes CdSe composite a potential candidate material for sensors development such as probe tips.

The heteroaggregation of GO with different minerals (montmorillonite, goethite, and kaolinite) in aqueous dispersions was investigated by Zhao et al. to gain an insight into the interactions of GO in aquatic systems, soil, and sediments [48]. Commercial graphite flakes were exfoliated via Hummers' method to obtain GO, and the commercial minerals were saturated with $Ca^{2+}$ and $Na^{+}$ by soaking in $CaCl_2$ and NaCl solutions. Mineral samples were introduced into GO dispersions, followed by prolonged shaking. In the pH range 4.0–8.5, GO and positively charged goethite formed heteroaggregates with multilayered structure, which resulted in enhanced dispersibility of the mineral due to electrostatic interactions. Also, the dissolved $Fe^{3+}$ ions of goethite did not destabilize GO suspension. On the other hand, GO showed no affinity towards montmorillonite or kaolinite.

## 4. Novel functional heterostructured materials

In this chapter, the main focus will be made on highly functional hybrid materials, which were prepared by heteroaggregation of individual particle systems, and they have proved as advantageous materials in certain applications. The latter point highlights the major difference

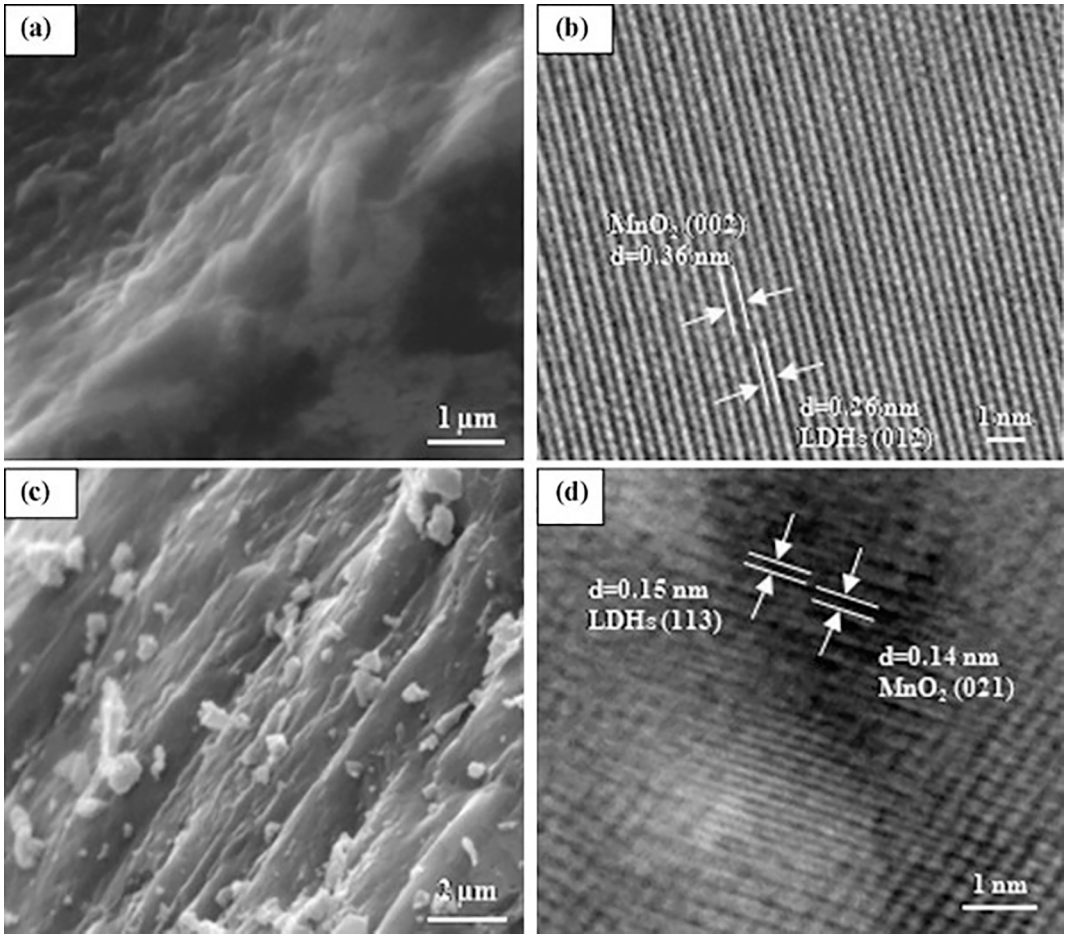


**Fig. 13.** SEM and high-resolution TEM images of nanocomposites obtained by (a, b) LBL method and (c, d) flocculated techniques [84]. Reprinted from (Fabrication and capacitance of NiFe-LDHs/$MnO_2$ layered nanocomposite via an exfoliation/reassembling process, 177 (1), Li, H.; Deng, L.; Zhu, G.; Kang, L.; Liu, Z.-H., *Mater. Sci. Eng. B,* 2012, 8–13). Copyright (2021), with permission from Elsevier.

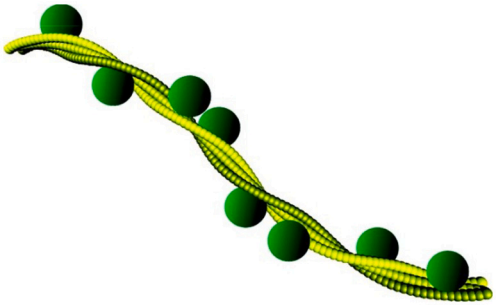

**Fig. 14.** Graphical representation of the fibril-polysaccharide complex prepared by heteroaggregation of β-lactoglobulin fibrils and globular clusters of κ-carrageenan (not to scale) [88]. Reprinted (adapted) with permission from (Jones, O. G.; Handschin, S.; Adamcik, J.; Harnau, L.; Bolisetty, S.; Mezzenga, R., Complexation of β-lactoglobulin fibrils and sulfated polysaccharides. *Biomacromolecules* 2011, 12 (8), 3056–3065). Copyright (2021) American Chemical Society.

between the present and previous chapters that the composites discussed below were used in real tests to assess their activity or performance.

### 4.1. Coating and packaging

Yan et al. prepared antioxidant films as packaging wrapper that help maintain the quality of food products and extend the shelf life without food preservatives [90]. The film material was prepared by adding different proportions of α-tocopherol-chitosan nanoparticles to a dispersion of chitosan-montmorillonite and the films were prepared by pouring the resulting composite onto square PTFE plates, which were later dried. The films showed 46.5% DPPH radical scavenging activity after 16 days of storage. Also, by coating sliced ham with the film solution, measurement of peroxide and TBARs values showed that the film possesses enhanced antioxidant activity for 120 days.

### 4.2. Antibacterial agents

Similar synthetic paths can be extended for preparing other functional materials such as antibacterial agents. For instance, Mallakpour and Hatami used Vitamin B9 (VB9) to prepare Ag@VB9-LDH composites as antibacterial agents [91]. The Ag nanoparticles were obtained by biofriendly synthesis using *R. officinalis* leaves, while VB9-MgAl-LDH was prepared by co-precipitation of the metal salts in the presence of VB9. Then, the Ag@VB9-LDH composite was prepared by mixing homogenous dispersions of Ag and VB9-MgAl-LDH. The resulting Ag@VB9-LDH composite was later incorporated in a chitosan biopolymeric matrix by mixing a water/acetic acid solution of chitosan with an aqueous dispersion of Ag@VB9-LDH to give chitosan/Ag@VB9-LDH composite. Both the Ag@VB9-LDH and the chitosan/Ag@VB9-LDH composites showed remarkable antibacterial activity against Gram-negative (*E. coli*) and Gram-positive (*S. aureus*), with the latter having greater inhibition zone diameter than with Ag@VB9-LDH. Fig. 16 shows FE-SEM images of

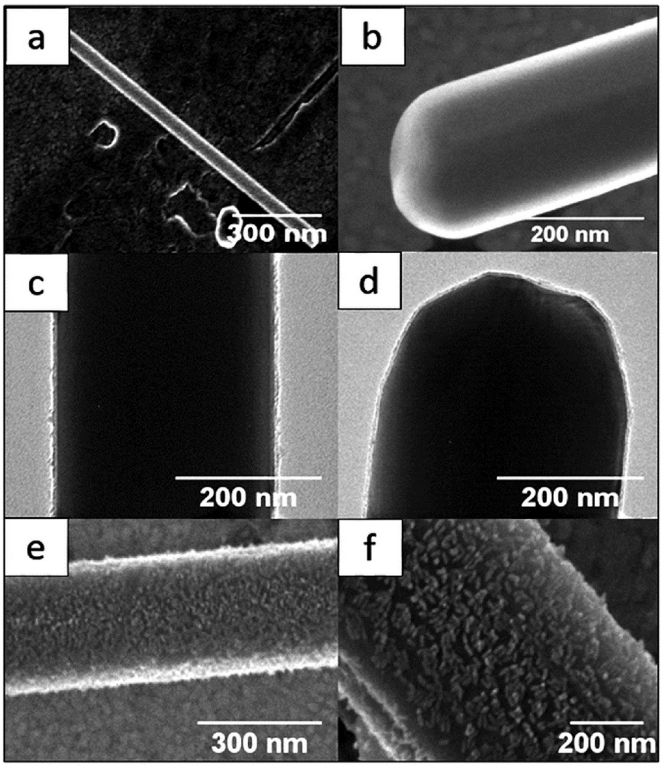


**Fig. 15.** Images of (a, b) Plain silver nanowires, (c, d) silver nanowires coated with silica, (e, f) silica coated silver nanowire coated with CdSe nanoparticles [89]. Reproduced from (Pita, I. A.; Singh, S.; Silien, C.; Ryan, K. M.; Liu, N., Heteroaggregation assisted wet synthesis of core-shell silver-silica-cadmium selenide nanowires. *Nanoscale*, 2016, 8 (2), 1200–1209) with permission from The Royal Society of Chemistry.

Ag@VB9-LDH and chitosan/Ag@VB9-LDH composite materials as well as pure LDH and chitosan.

Precillia et al. developed a GO/NiO composite that acted as an antibacterial agent against Methicillin Resistant *Staphylococcus aureus* and *A. baumannii* and as a potential fluorescent chemosensor for leucine. GO was prepared by the Hummers method and NiO NPs were synthesized via co-precipitation of the metal salt. The GO/NiO composite was prepared by prolonged mixing of well-dispersed aqueous dispersions of GO and NiO nanoparticles under reflux. The composite was more sensitive towards *A. baumannii* than *Staphylococcus aureus,* as indicated by the minimum inhibitory zone concentration (400 μg/ mL for *Staphylococcus aureus* and 200 μg/mL for *A. baumannii*). Fluorescence analysis also indicated that the composite selectively detects leucine, even in the presence of other amino acids, through photo-induced electron transfer mechanism [92].

Almasi et al. fabricated an antimicrobial nanocomposite by impregnation of commercial CuO NPs into bacterial cellulose nanofibers (BCNF) as well as chitosan nanofibers (CHNF) [93]. The BCNF were produced by *Gluconacetobacter xylinus* culture, while CHNF obtained by the deacetylation of shrimp shell chitin through chemical treatments. The CuO-CHNF was prepared by mixing an aqueous CuO dispersion (contained 1% (v/v) acetic acid) with a dry base of CHNF followed by ultrasonic homogenization. The composite was obtained by filtration and subsequent drying. On the other hand, the CuO-BCNF composite was prepared similarly, but the CuO NPs were dispersed in water rather than 1% (v/v) acetic acid solution. The hybrid materials were formed via hydrogen bonds between organic and inorganic phases. While the crystalline structure of BCNF was preserved after CuO impregnation, CHNF underwent substantial changes in crystallinity with increased amorphous region. The CuO NPs antibacterial activity against both Gram-positive and Gram-negative bacteria decreased upon attachment to BCNF, while CHNF was more effective than BCNF in release controlling of CuO NPs to water.

### 4.3. Catalysis

Ben Moussa et al. prepared a bi-functional catalyst for selective n-heptane hydrocracking [46]. Two-domain $Al_2O_3$/zeolite composite was prepared by dropwise mixing of stable suspensions of β-zeolite and commercial boehmite (γ-AlOOH nanoparticles) under vigorous stirring, and the obtained solid phase was calcined. The second composite of $Al_2O_3$/zeolite, characterized by larger zeolite domain, was prepared by wet mechanical mixing. Then, by adjusting the pH and Pt precursors, Pt nanoparticles were selectively deposited onto either $Al_2O_3$ or zeolite domains, as shown in Fig. 17, with a soft thermo-reduction step was applied to obtain a composite Pt/$Al_2O_3$-zeolite with a well-dispersed Pt phase. The location of the Pt nanoparticles and the size of the zeolite domains did not significantly modify the conversion of n-heptane hydro isomerization. However, the location of Pt nanoparticles on zeolite/alumina aggregates impacted the selectivity of the resulting catalyst.

Li et al. synthesized a series of catalytic composites of NiAl-LDH decorated with captopril-capped $Au_xPd_y$ nanoclusters (NCs) with multiple Au/Pd ratios; the composites exhibited higher aerobic oxidation activity of 1-phenylethanol than monometallic NCs depending on the ratio [94]. The NiAl-LDH was prepared by the co-precipitation method, while bimetallic captopril-capped $Au_xPd_y$ NCs was synthesized by size-focusing synthetic strategy using $Na_2PdCl_4$ and $HAuCl_4{\cdot}4H_2O$. The NiAl-LDH/$Au_xPd_y$ hybrid was prepared by the addition of captopril-capped $Au_xPd_y$ solid to an aqueous dispersion of NiAl-LDH under vigorous stirring (Fig. 18) followed by calcination. The catalytic activities increased and then decreased with decreasing the Au/Pd ratios from 24 to 1.56; the $Au_{87}Pd_{13}$/NiAl-LDH with a size of 1.5 ± 0.5 nm showed the highest activity with a turnover frequency of 6810 $h^{-1}$ and 131,400 $h^{-1}$ in toluene and under solvent-free conditions, respectively. The catalyst showed high suitability to alcohol substrates and maintain 98% of the initial conversion of 1-phenylethanol after 10 cycles.

### 4.4. Photocatalysis

Li et al. reported the synthesis of catalytic magnetite core/$W_7O_{24}^{6-}$-LDH shell nanocomposite [95]. Magnetite particles were synthesized using the solvent-thermal method and were further coated with silica via the sol-gel process. The silica-coated magnetic particles were further coated with 20 bilayers of $CO_3^{2-}$/LDH by alternate additions of the particles into aqueous solutions of $Na_2CO_3$ and formamide-based suspensions of $W_7O_{24}^{6-}$-LDH nanosheets. The mixture was sonicated, and the solid particles were collected by centrifugation before introduction into the next solution/suspension. After that, the sample was ramp-heated under $N_2$ atmosphere to remove water as well as $CO_3^{2-}$ ions, and then was dispersed in water to recover the original LDH structure. The composite structure showed high anion loading capacity as well as catalytic activity towards the photodegradation of trace hexachlorocyclohexane in aqueous solutions and could effectively be recycled and reused up to six times without any apparent decrease in its catalytic activity.

Zhu et al. prepared a catalytic nanocomposite of black phosphorous (BP) nanosheets loaded with bismuth vanadate ($BiVO_4$) nanosheets for water splitting applications [96]. BP nanoflakes were prepared through the exfoliation method in a *N*-methyl-2-pyrrolidone (NMP) solution, while $BiVO_4$ nanosheets were synthesized using the hydrothermal method in the presence of sodium dodecylbenzenesulfonate. Then BP and $BiVO_4$ nanosheets were easily hybridized by electrostatic interactions. The BP/$BiVO_4$ heterostructures were prepared by adding $BiVO_4$ solid sample into BP/NMP dispersion followed by prolonged sonication and stirring. The UV–Vis diffuse reflectance spectra and Mott-Schottky plots indicated that BP/$BiVO_4$ heterostructures can be used as *Z*-scheme photocatalysts. Substantial amounts of $H_2$ and $O_2$ were

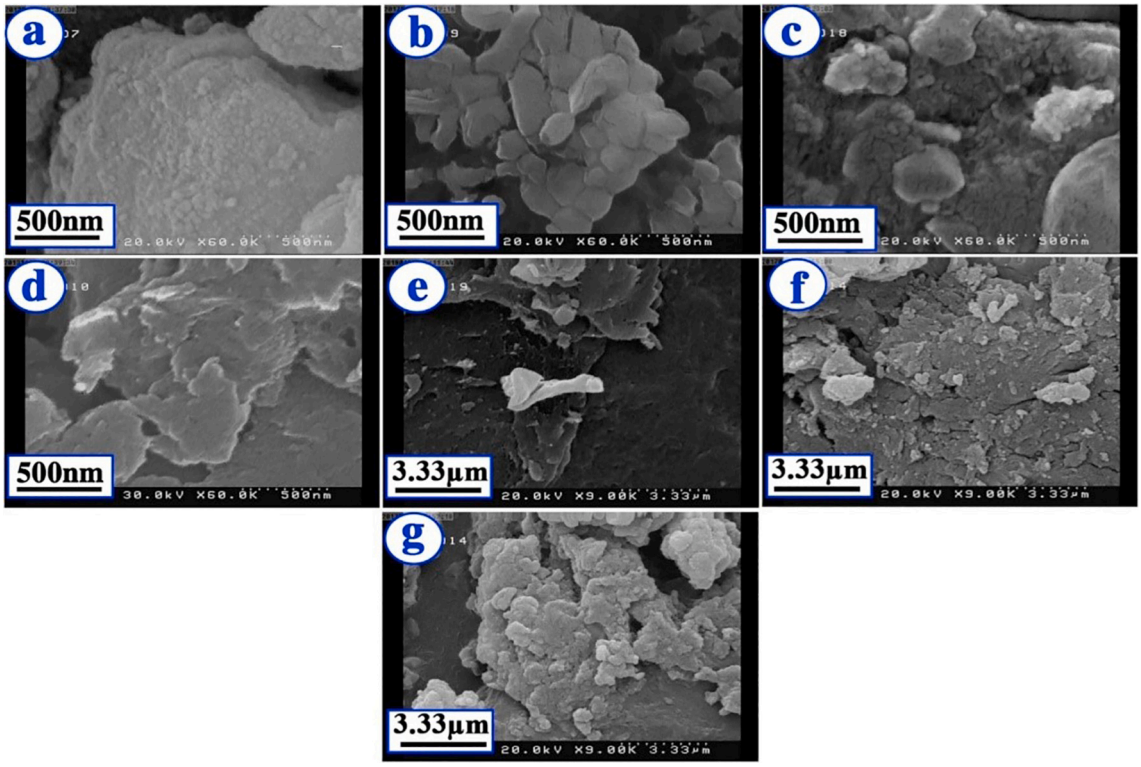


**Fig. 16.** FE-SEM images of (a) pure LDH (b) VB9-LDH and (c) Ag@VB9-LDH (d) pure chitosan and chitosan/Ag@VB9-LDH with (e) 3 wt% (f) 6 wt% and (g) 9 wt% of Ag@VB9-LDH [91]. Reprinted from (Green and eco-friendly route for the synthesis of Ag@Vitamin B9-LDH hybrid and its chitosan nanocomposites: Characterization and antibacterial activity, 154, Mallakpour, S.; Hatami, M., *Polymer*, 2018, 188–199). Copyright (2021), with permission from Elsevier.

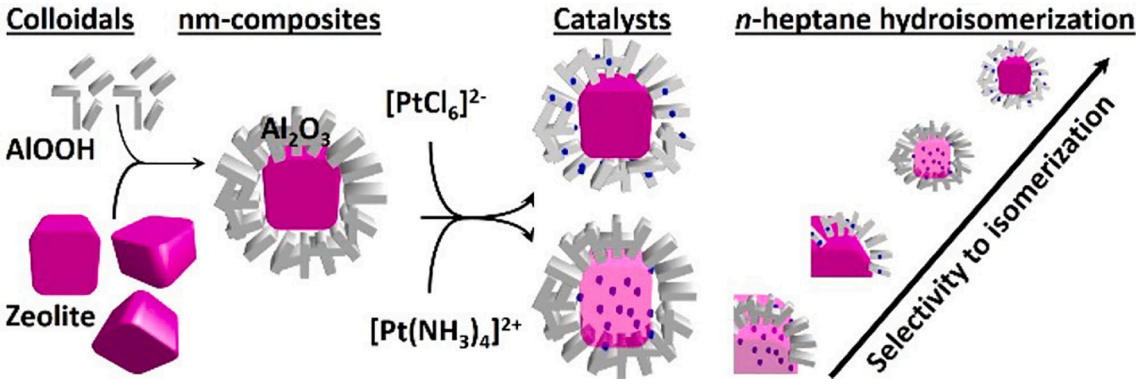


**Fig. 17.** Schematic representation of the synthesis and catalytic role of the two-domain $Al_2O_3$/zeolite composite [46]. Reprinted (adapted) with permission from (Ben Moussa, O.; Tinat, L.; Jin, X. J.; Baaziz, W.; Durupthy, O.; Sayag, C.; Blanchard, J., Heteroaggregation and selective deposition for the fine design of nano-architectured bifunctional catalysts: Application to hydroisomerization. *ACS Catal.* 2018, 8 (7), 6071–6078). Copyright (2021) American Chemical Society.

detected under visible light irradiation in the presence of BP/$BiVO_4$ without sacrificial agents, whereas neither BP nor $BiVO_4$ alone could catalyse water-splitting reaction.

Gunjakar et al. reported the preparation of catalytic mesoporous nanohybrid of co-stacked oppositely charged nanosheets of layered titanate and ZnCr-LDH [97]. The former was prepared by conventional solid-state reaction, while the latter was obtained by direct co-precipitation. The heterolayered nanohybrid was synthesized by mixing the formamide suspensions of ZnCr-LDH and layered titanate under constant stirring. The restacked nanohybrid was retrieved by centrifugation, washing, and vacuum-drying. The porosity could be controlled by changing the ratio of layered titanate/ZnCr-LDH, and the heterolayered nanohybrid showed enhanced chemical stability as well as better catalytic activity in the visible light-induced $O_2$ generation compared to pristine ZnCr-LDH material.

Szabó et al. prepared $TiO_2$-GO composites with photocatalytic activity towards the decomposition of pollutants, and with accelerated sedimentation properties [98]. The GO was prepared from commercial graphite by Brodie method while $TiO_2$ nanoparticles were obtained commercially. The $TiO_2$-GO composites were formed by addition of well-dispersed GO suspensions into aqueous dispersions of $TiO_2$, upon which the system is generated within seconds. The $TiO_2$-GO composite could catalyse the photo-oxidation of the phenols, as test pollutants, and possessed good recyclability that could be exploited in large scale treatment of wastewater. Compared to pure $TiO_2$, the presence of GO caused some loss of photocatalytic efficiency but induced an accelerated sedimentation leading to complete separation of the photocatalyst from the reaction mixture.

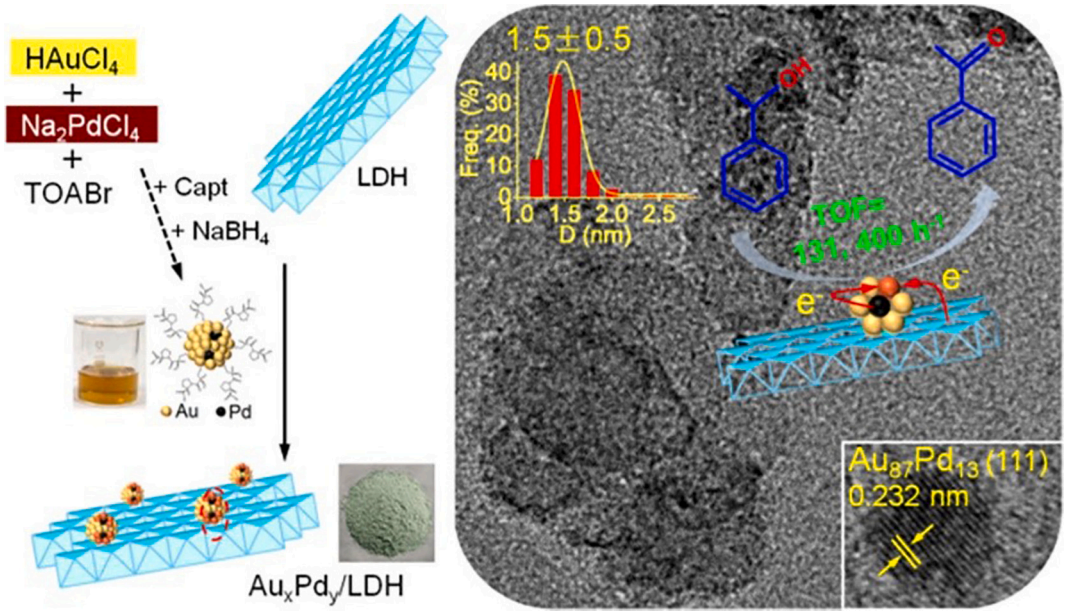


**Fig. 18.** (Left) Scheme of synthesis and structure of $Au_xPd_y$/LDH, (right) HRTEM image with the catalytic activity and size distribution of $Au_{87}Pd_{13}/Ni_3Al$-LDH [94]. Reprinted (adapted) with permission from (Li, J.; Xu, Y.; Wang, S.; Zhang, H., Ultrafine AuPd nanoclusters on layered double hydroxides by the capt-capped AuPd cluster precursor method: Synergistic effect for highly efficient aerobic oxidation of alcohols. *J. Phys. Chem. C,* 2019, 123 (25), 15,483–15,494). Copyright (2021) American Chemical Society.

In another work, Patzkó et al. prepared ZnO/ZnAl-LDH as a catalyst for phenol photo-oxidation [99]. Initially, the ZnAl-LDH was prepared from $Zn(CH_3CO_2)_2.2H_2O$ and $Al(NO_3)_3$ while the $Zn(OH)_2$ was prepared by hydrolysis. Then, $Zn(OH)_2$ was intercalated into the LDH layers by mixing the corresponding dispersions, and the obtained solid was calcined at different temperatures to obtain the ZnO phase from $Zn(OH)_2$. The composite showed remarkable catalytic properties in phenol photo-oxidation in aqueous solutions. The calcination did not affect the catalytic activity significantly; however, the ratio of Zn/Al affected the phenol degradation rate, which peaked when a ratio of 4:1 was applied in the reaction mixture. Fig. 19 shows the heteroaggregation of LDH with ZnO nanoparticles and the structure of the ZnO/LDH nanocomposites after calcination.

Boppella et al. prepared reduced GO-$La_2Ti_2O_7$/NiFe-LDH composite with remarkable photocatalytic activity towards $H_2$ evolution under simulated light irradiation without expensive Pt co-catalyst [100]. The reduced GO (rGO), NiFe-LDH, and $La_2Ti_2O_7$ (LTO) nanosheets were synthesized via modified Hummers method, co-precipitation method, and hydrothermal synthesis, respectively, while the rGO-LTO was prepared by dissolving the relevant solids in an aqueous medium followed by the thermal treatment in an autoclave. Finally, the rGO-LTO/NiFe-LDH was prepared by heteroaggregation of rGO-LTO and NiFe-LDH by mixing dispersions of the corresponding components in an ultrasonic bath. Fig. 20 shows TEM and HR-SEM images of the prepared composite as well as bare components. The $H_2$ production rate of the novel rGO/LTO/NiFe heterostructure was 9 times higher than that of pure LTO, which can be attributed to the synergistic effect of rGO and NiFe-LDH. The composite also showed a minimal loss in activity after 4 runs, and the heterojunctions were stable under solar irradiation.

Mallakpour and Hatami reported the preparation of catalytic MgAl-LDH/Vitamin B9/$TiO_2$ nanoparticles (LDH-VB9/$TiO_2$) hybrid [101]. Commercially obtained VB9 was first intercalated into MgAl-LDH during the co-precipitation synthesis of the LDH. Aqueous dispersions of LDH-VB9 and commercial $TiO_2$ nanoparticles were mixed and the resulting dispersion was then ultrasonicated, where the $TiO_2$ nanoparticles were dispersed on the surface of the VB9-intercalated LDH layers. To enhance its physicochemical properties, the LDH-VB9/$TiO_2$ composite was introduced as a filler into a matrix of crosslinked poly (vinyl alcohol). The composites showed photodegradation potential of methylene blue (MB) dye under ultraviolet illumination. The rate constant of photodegradation by LDH-VB9-$TiO_2$ was higher than that catalysed by pure $TiO_2$ as well as by the composite in poly(vinyl alcohol). The LDH-VB9-$TiO_2$ also showed a remarkable half-life for degradation of MB dye, compared to that without photocatalyst, and thus, can be utilized in many industrial applications such as water purification.

Evidently, owing to the complexity and requirements of the catalytic application processes, hybrid catalytic systems offer numerous advantages and are much more robust than their single-component counterparts. For example, heteroaggregated catalytic composites have better selectivity, higher activity due to sustained catalytic surface, and recyclability when incorporated with magnetic materials [102,103]. Polymer matrix composite catalysts have enhanced physicochemical properties such as electronic and thermomechanical features. The hybridization also influences the rate of adsorption/desorption and diffusion of molecules, and thus enables the control over the kinetics of the catalytic reactions [104]. Lastly, the incorporation of macropores into catalytic systems minimizes diffusion barriers and results in uniform distribution of active sites, it also increases light scattering and multiple internal reflections in photocatalytic materials resulting in improved photocatalytic efficiency [105].

### 4.5. Removal of contaminant materials

Zong et al. prepared a hollow MgFe-layered double oxide (LDO) using carbon spheres (CSs) as cores. The hollow MgFe-LDO spheres were effective in the adsorption and removal of methylene blue [106]. The MgFe-LDO and CSs were prepared by co-precipitation and hydrothermal synthesis, respectively. Then, solid samples of CSs were added to aqueous dispersions of MgFe-LDO shell under ultrasonic irradiation, where the composite forms due to electrostatic heteroaggregation, and the obtained composites were then calcined to burn the carbon component and form hollow MgFe-LDO. Fig. 21 shows SEM and TEM images with the EDX elemental mapping of CSs, CSs@MgFe-LDHs and hollow MgFe-LDO. The efficient hollow material showed high adsorption capacity and rapid adsorption of methylene blue compared to ordinary LDO due to abundant and highly accessible active sites for

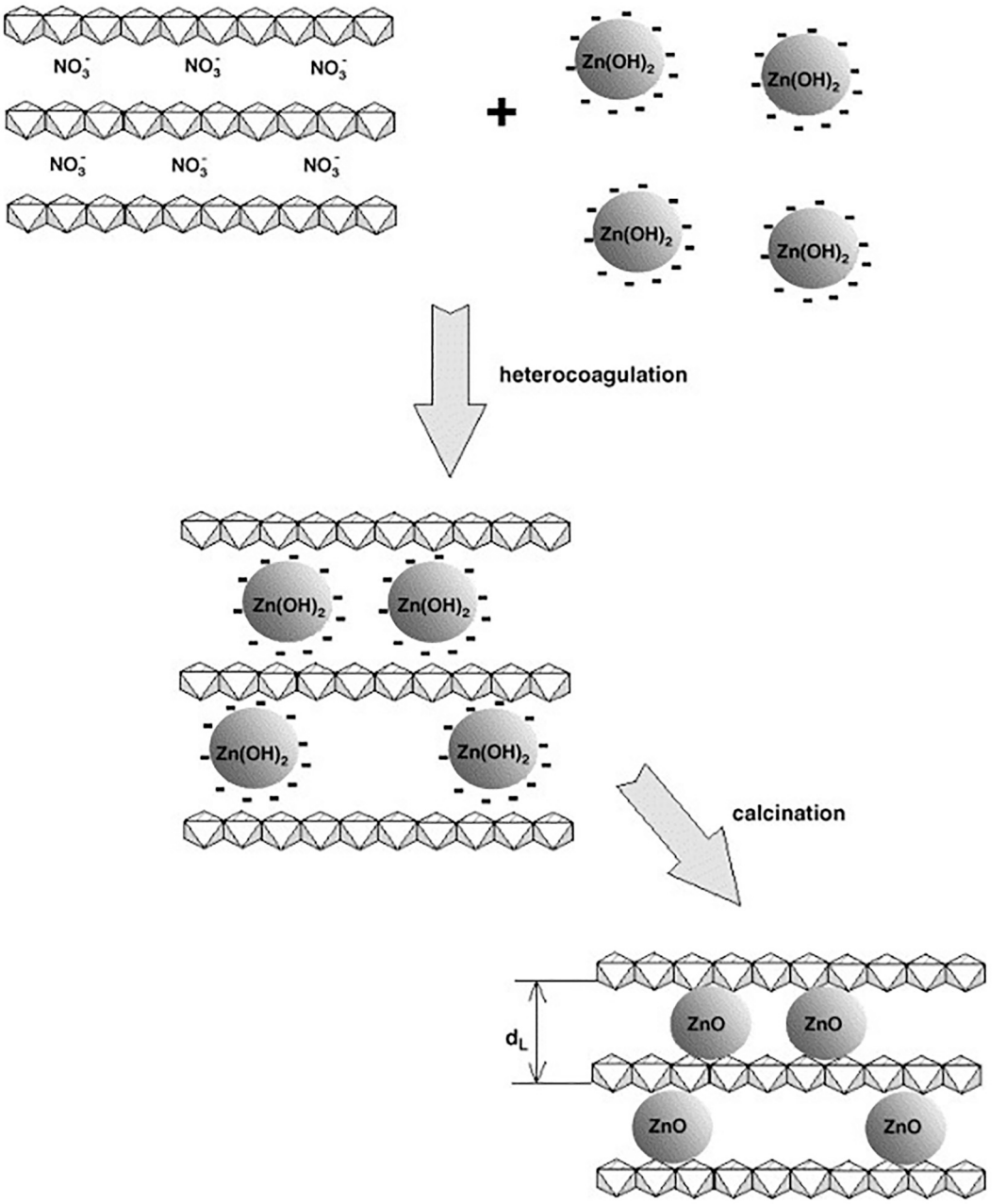


**Fig. 19.** Heterocoagulation of LDH with ZnO nanoparticles from stable dispersions and the structure of the ZnO/LDH nanocomposites after calcination [99]. Reprinted from (ZnAl-layer double hydroxides as photocatalysts for oxidation of phenol in aqueous solution, *265* (1–3), Patzko, A.; Kun, R.; Hornok, V.; Dekany, I.; Engelhardt, T.; Schall, N., *Colloids Surfaces A-Phys. Eng. Asp.,* 2005, 64–72). Copyright (2021), with permission from Elsevier.

adsorption, which occurred in a monolayered manner by chemical interactions. Additionally, the LDO was stable for at least five cycles and could be simply recycled via a magnet due to the presence of magnetic Fe.

Hu et al. reported the preparation of a novel nanocomposite for adsorption of RY2 dye from wastewater [107]. The composite was prepared by the heteroaggregation of MgAl-LDH nanoparticles and Na-modified bentonite sheets by mixing the relevant dispersions at different mass ratios, followed by calcination. The MgAl-LDH was prepared by co-precipitation under alkaline conditions, while bentonite was obtained commercially. The bentonite was further modified by soaking in 1 M NaCl solution to replace its exchangeable cations by $Na^{+}$ cations. Fig. 22 shows SEM images of bentonite and LDH-bentonite hybrid. The dye uptake capacity increases with the increase in LDH loading in the hybrid, reaching 100% with a LDH/bentonite ratio of 2.3:1. For the same ratio, the calcined sample showed better removal performance compared to uncalcined hybrids, and smaller LDH particles showed better removal ability owing to the larger surface area.

Gong et al. reported the preparation of a nanocomposite by attaching LDH nanocrystals onto carbon nanospheres (CNs) for removal of heavy metal ions such as $Cu^{2+}$, $Cd^{2+}$, and $Pb^{2+}$ from water [108]. The LDH was synthesized in pure methanol using $Mg^{2+}$ and $Al^{3+}$ salts, and the CNs was prepared through glucose carbonization under hydrothermal conditions in an aqueous media. The methanol-based suspensions of LDH and CNs were then mixed and ultrasonicated to obtain LDH@CNs nanocomposite, which was collected by centrifugation followed by drying. Fig. 23 shows TEM images of the LDH@CNs composite and its bare constituents. The heavy metal removal efficiency of LDH@CNs nanocomposite was much larger than that of any of its bare constituents. Removal efficiency of $Cu^{2+}$, $Cd^{2+}$, and $Pb^{2+}$ by LDH@CNs was 99.7%,

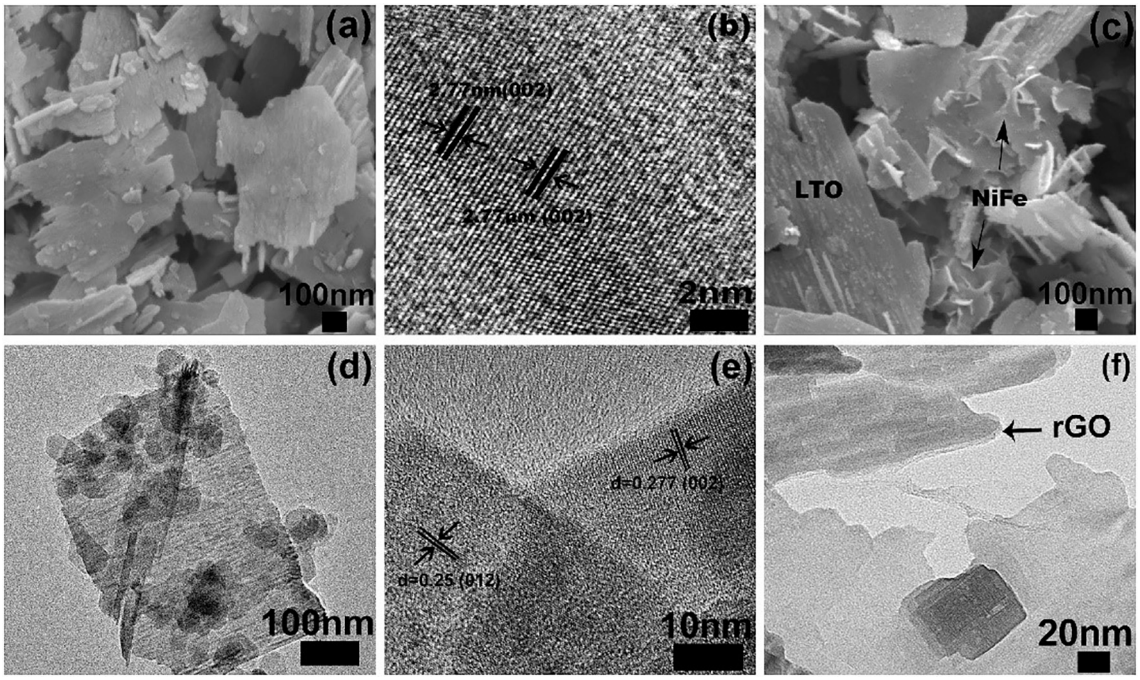


**Fig. 20.** Electron microscopy images. (a) HR-SEM image of LTO, (b) HR-TEM image of LTO, (c) HR-SEM image of LTO/NiFe-LDH, (d) TEM image of LTO/NiFe-LDH, (e) HR-TEM image of LTO/NiFe-LDH and (f) HR-TEM image of rGO/LTO. [100]. Reprinted from (Spatial charge separation on strongly coupled 2D-hybrid of rGO/La2Ti2O7/NiFe-LDH heterostructures for highly efficient noble metal free photocatalytic hydrogen generation, 239, Boppella, R.; Choi, C. H.; Moon, J.; Kim, D. H., *Appl. Catal. B-Environ.* 2018, 178–186). Copyright (2021), with permission from Elsevier.

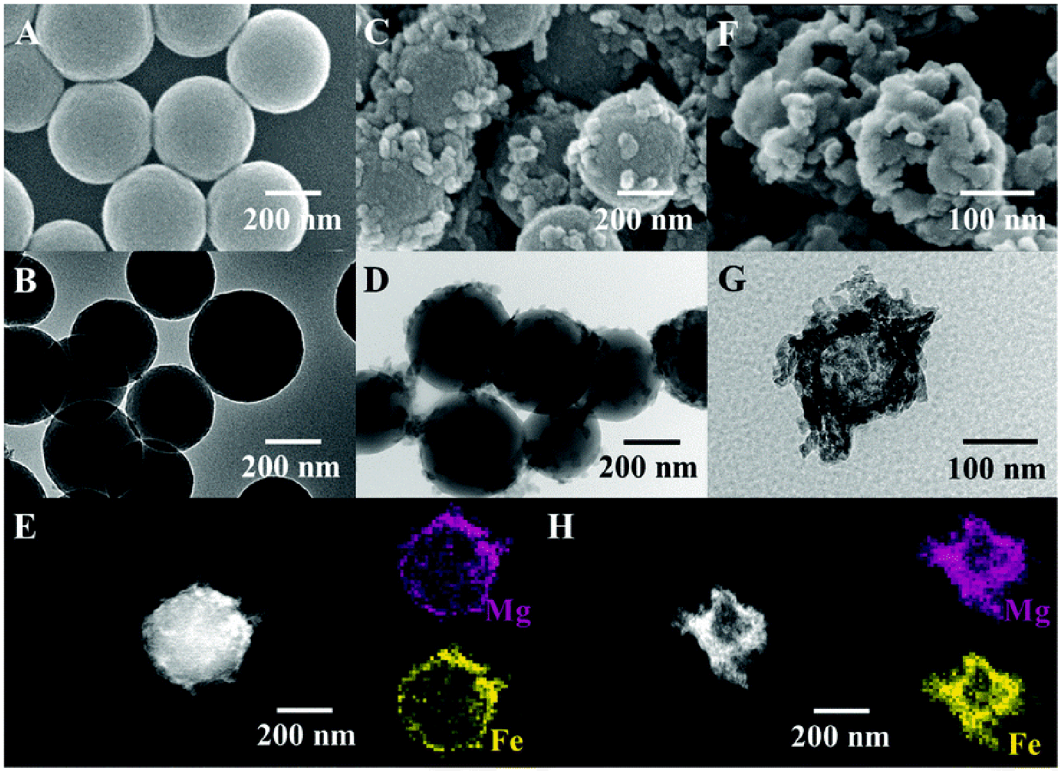


**Fig. 21.** SEM and TEM images of (A, B) CSs, (C, D) CSs@MgFe-LDHs and (F, G) hollow MgFe-LDO. The EDX elemental mapping results of (E) CSs@MgFe-LDHs and (H) hollow MgFe-LDO [106]. Reproduced from (Zong, Y. T.; Li, K. T.; Tian, R.; Lin, Y. J.; Lu, C., Highly dispersed layered double oxide hollow spheres with sufficient active sites for adsorption of methyl blue. *Nanoscale*, 2018, 10 (48), 23,191–23,197) with permission from The Royal Society of Chemistry.

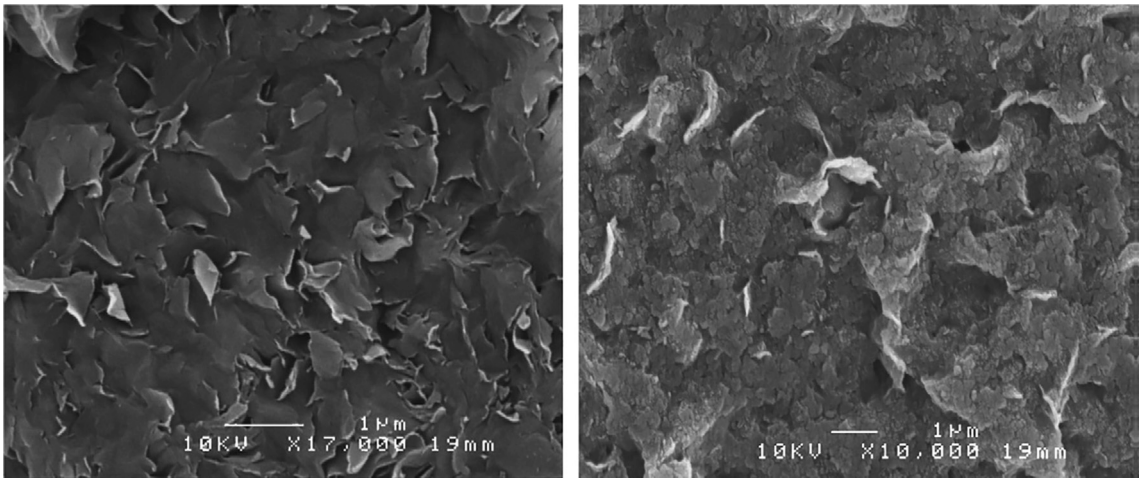


**Fig. 22.** SEM images of (left) bentonite and (right) LDH-bentonite hybrid [107]. Reprinted from (A novel colour removal adsorbent from heterocoagulation of cationic and anionic clays, 308 (1), Hu, Q. H.; Xu, Z. P.; Qiao, S. Z.; Haghseresht, F.; Wilson, M.; Lu, G. Q., *Journal of Colloid and Interface Science*, 2007, 191–199). Copyright (2021), with permission from Elsevier.

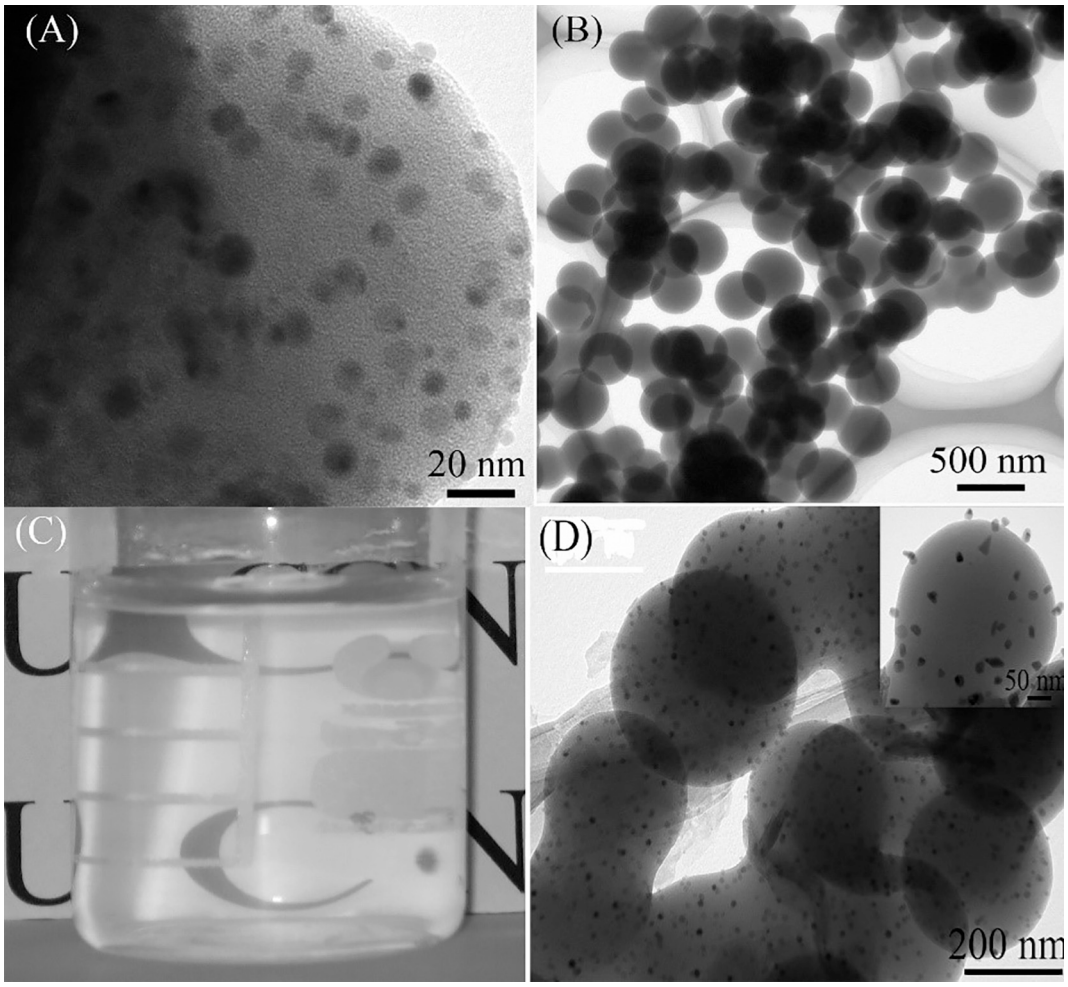


**Fig. 23.** TEM images of (A) LDH, (B) CNs, and (D) the assembly of LDH@CNs composites. (C) A translucent and stable suspension of LDH in methanol/water solvent [108]. Reprinted (adapted) with permission from (Gong, J. M.; Liu, T.; Wang, X. Q.; Hu, X. L.; Zhang, L. Z., Efficient removal of heavy metal ions from aqueous systems with the assembly of anisotropic layered double hydroxide nanocrystals@carbon nanosphere. *Environ. Sci. Technol.* 2011, 45 (14), 6181–6187). Copyright (2021) American Chemical Society.

89.3%, and 55.4%, respectively, and the maximum adsorption capacity was ~19.9, ~17,5, and ~ 12.5 mg/g, respectively, when the nanocomposite concentration was 10 mg/L. The order of removal $Cu^{2+}$ > $Cd^{2+}$ > $Pb^{2+}$ can be attributed to closeness in atomic radii to the constituent ions of LDH.

Zhang et al. prepared a three-component composite by immobilizing magnetite ($Fe_3O_4$) and MgAl-LDH particles onto GO sheets for removal of emulsified oils in water/oil systems [109]. The GO was synthesized by a modified Hummers and Offeman method, while magnetite-GO (MGO) hybrids were prepared by co-precipitating magnetite in the presence of GO. The MgAl-LDH precursor with a Mg/Al molar ratio of 3:1 was prepared by a co-precipitation method. The adsorbent composite MGO/MgAl-LDH was prepared by addition of LDH to a MGO suspension followed by sonication, the electrostatic attraction and hydrogen bonding enabled the heteroaggregation of LDH and MGO. Several composites with different LDH/MGO ratios were prepared. The hybrid materials retained oil removal efficiencies of 95.14%, 96.26%, and 97.88% for crude oil, white oil, and decane, respectively, after five cycles. The efficiency increased with the ionic strength and was also affected by the LDH/MGO ratio, where the highest removal potential was observed when the ratio was 1:1 for crude oil and 1:3 for white oil and decane. Fig. 24 shows the schematic preparation and structure of the composite as well as the removal action of MGO/MgAl-LDH hybrid.

Zubitur et al. studied the heteroaggregation between carbon black pigment particles with various polymeric particles, prepared by dispersion polymerization of poly(methyl methacrylate), polystyrene, poly(n-butyl acrylate), and other *co*-polymers [110]. Samples of 5% (w/w) dry pigment were added to methanol, ethanol, or water dispersions of the polymeric latex particles at different pigment ratios and were further sonicated to allow the pigment particles to be immobilized on the polymeric surface by heteroaggregation via acid-base interactions owing to the acidic and basic sites on carbon black. Carbon black adsorbs more uniformly in methanol and ethanol compared to water, and the adsorption was not affected by the different functional groups on the various polymeric particles.

### 4.6. Optical materials

Lee et al. prepared a highly light scattering composite material by coating commercial PS particles with Au NPs and Ag nanocubes (NCs) [111]. The Au NPs and Ag NCs of various sizes were separately prepared and were further capped with PVP. Volumes of aqueous dispersions of latex and metal particles were mixed, followed by dropwise addition of tetrahydrofuran (THF) until the suspension has a THF concentration of 50% (v/v). By adjustments in the amount of added THF, not only homoaggregation could be avoided, but the coating morphology, metal coverage, and optical properties of the composite could be tuned. Smaller Au NPs resulted in continuous and close-packed metal coatings and possessed optical properties resembling those for complete shells. Larger Au NPs and Ag NCs, however, resulted in less dense coatings and higher scattering properties. Raman spectroscopy indicated the Au and Ag composites, especially Ag NCs-latex, exhibited highly enhanced Raman signals of PVP molecules and thus, can be used as effective SERS substrates. This result enables their use in biomedical imaging, sensors, photonics, and electronics. Fig. 25 shows SEM images of the obtained AuNP-Ps hybrid.

### 4.7. Bioactive materials

Deák et al. heteroaggregated ZnMgAl-LDH and Ag NPs-loaded montmorillonite lamellae [112]. The former particles were prepared by the co-precipitation method, while the Ag NPs-montmorillonite lamellae were prepared by synthesis of Au NPs in the presence of montmorillonite. The LDH-Ag-montmorillonite composite was prepared by dissolving a sample of the prepared LDH solid in an aqueous dispersion of Ag NPs-montmorillonite. As shown in Fig. 26, the composite behaved like coherent gels at low pH (≲4.5) and incoherent sols at higher pH (≳4.5). The hybrid material was synthesized with composition that allows a sol-gel transition. The composite was suitable for the release of the immobilized antimicrobial Ag NPs via a pH-controlled gel-sol transition. The pH-responsive property in LDH-Ag-montmorillonite

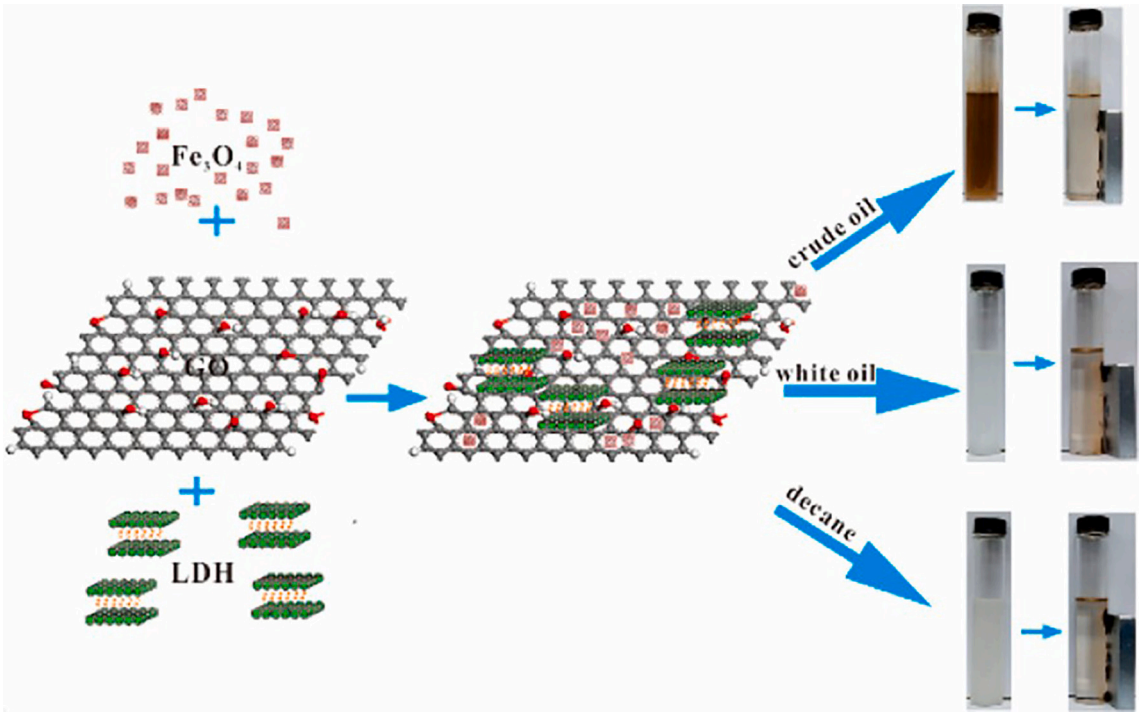


**Fig. 24.** Structure and removal activity of MGO/MgAl-LDH composites with crude oil, while oil and decane [109]. Reprinted (adapted) with permission from (Zhang, B.; Hu, R. T.; Sun, D. J.; Wu, T.; Li, Y. J., Fabrication of magnetite-graphene oxide/MgAI-layered double hydroxide composites for efficient removal of emulsified oils from various oil-in-water emulsions. *J. Chem. Eng. Data,* 2018, 63 (12), 4689–4702). Copyright (2021) American Chemical Society.

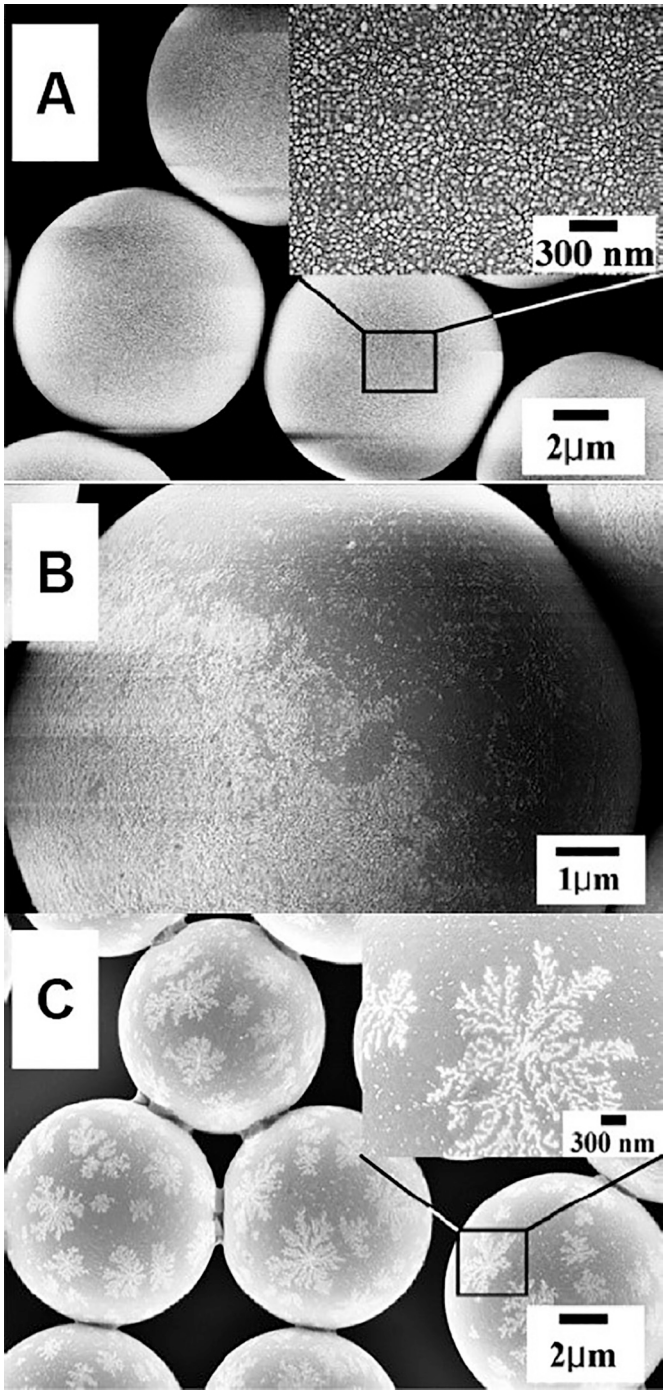


**Fig. 25.** SEM images of 30 nm AuNP-Ps hybrid obtained from (A) 50 vol% THF-water solution (B) 70 vol% THF-water solution (C) 50 vol% THF-water solution with fewer NPs compared to (A) [111]. Reprinted (adapted) with permission from (Lee, J. H.; Mahmoud, M. A.; Sitterle, V. B.; Sitterle, J. J.; Meredith, J. C., Highly scattering, surface-enhanced Raman scattering-active, metal nanoparticle-coated polymers prepared via combined swelling-heteroaggregation. *Chem. Mat.* 2009, 21 (23), 5654–5663). Copyright (2021) American Chemical Society.

enabled their application in biological systems that have acidic pH under normal conditions but become basic in case of abnormalities such as bacterial infection.

Lui et al. reported a novel $CeO_2$-$Fe_3O_4$@LDH bio-nanocomposite [113]. The polyacrylic acid (PAA)-stabilized $CeO_2$ and $Fe_3O_4$ NPs were prepared by precipitation and co-precipitation, respectively. The

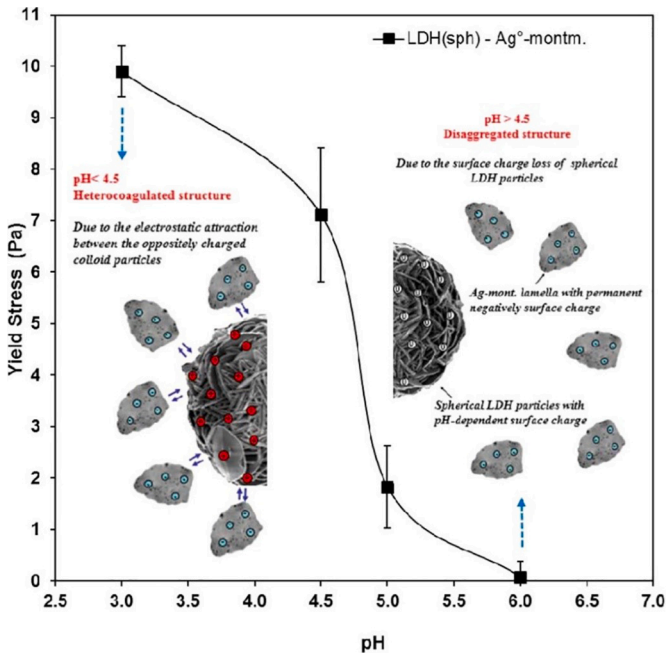


**Fig. 26.** The pH-dependent sol-get transition of LDH-Ag-montmorillonite composite. Above pH 4.5, a disaggregated structure is observed due to loss of surface charge. At pH below 4.5, heteroaggregated structure was maintained due to electrostatic attraction between the building blocks [112]. Reprinted (adapted) with permission from (Deak, A.; Janovak, L.; Tallosy, S. P.; Bito, T.; Sebok, D.; Buzas, N.; Palinko, I.; Dekany, I., Spherical LDH-Ag°-montmorillonite heterocoagulated system with a pH-dependent sol-gel structure for controlled accessibility of AgNPs immobilized on the clay lamellae. *Langmuir*, 2015, 31 (6), 2019–2027). Copyright (2021) American Chemical Society.

MgAl-LDH was prepared by co-precipitation followed by hydrothermal treatment. The $CeO_2$-$Fe_3O_4$@LDH nanocomposite was prepared by adding a certain volume of the LDH suspension dropwise into an aqueous mixture of $CeO_2$ and $Fe_3O_4$ NPs under continuous stirring, where electrostatic forces between the NPs and LDH led to the composite formation. The novel biocompatible nanocomposite has shown great potential as an antioxidant for reactive oxygen species (ROS) scavenging in macrophages with no cytotoxicity to either macrophages or CHO cells at concentrations where ROS scavenging is significant. In MRI application, the composite exhibited a good magnetic resonance signal in the macrophages, making it a potential contrast agent for cell imaging processes. These functionalities are demonstrated in Fig. 27.

Darabdhara et al. prepared graphitic carbon nitride (g-$C_3N_4$) nanosheets decorated with bimetallic Au-Ni NPs. The g-$C_3N_4$ nanosheets were prepared by calcination of urea, and the resulting g-$C_3N_4$ sample was dispersed in a mixture of ethanol/hexane by ultrasonication. The Au-Ni bimetallic nanoparticles were synthesized by solvothermal reduction technique using Ni(acetylacetonate)$_2$ and $HAuCl_4 \cdot 3H_2O$ precursors, and the collected Au-Ni nanoparticles were dispersed in hexane. Then, dispersions of g-$C_3N_4$ were mixed with the Au-Ni NPs dispersion to obtain the Au-Ni/g-$C_3N_4$ nanocomposite, which showed intrinsic peroxidase activity towards a number of substrates such as 3,3′,5,5′-tetramethylbenzidine (TMB) and 2,2′-azino-bis(3-ethylbenzthiazoline-6-sulphonic acid) (ABTS) in presence of $H_2O_2$, which enabled its incorporation into colorimetric glucose detection system with glucose oxidase with a detection limit of 1.7 μM and a linear detection range of 0.5 to 30 μM [114]. Monometallic Au/g$C_3N_4$ and Ni/g-$C_3N_4$ nanocomposites, on the other hand, showed a detection limit of 3.55 and 6.23 μM, respectively. The nanocomposites showed no cytotoxic towards HUVEC cell line, which rendered them biocompatible and suitable for biosensor applications.

Zhao developed a biosensor based on nanocomposite carrier and

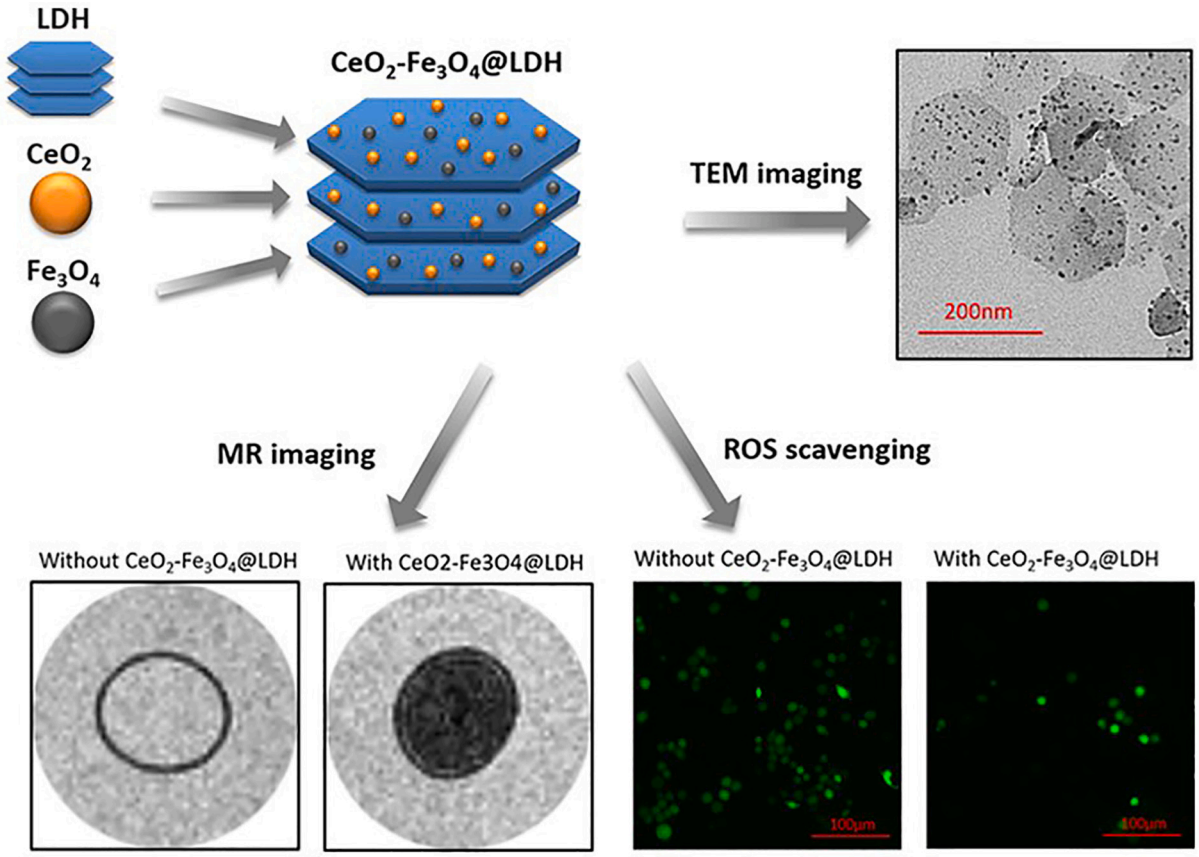


**Fig. 27.** Schematic representation of the expected structure of $CeO_2$-$Fe_3O_4$@LDH nanocomposite. TEM imaging confirms the immobilization of $CeO_2$ and $Fe_3O_4$ NPs onto the LDH platelets. The MRI signal, corresponding to darker colour, could be detected in presence of the nanocomposite. Macrophages, stimulated by $H_2O_2$, generate excessive ROS and exhibit green fluorescence signal, which was significantly reduced 1 day after treatment with $CeO_2$-$Fe_3O_4$@LDH nanocomposite [113]. Reprinted (adapted) with permission from (Liu, Y.; Wu, Y.; Zhang, R.; Lam, J.; Ng, J. C.; Xu, Z. P.; Li, L.; Ta, H. T., Investigating the use of layered double hydroxide nanoparticles as carriers of metal oxides for theranostics of ROS-related diseases. *ACS Appl. Bio Mater.* 2019, 2 (12), 5930–5940). Copyright (2021) American Chemical Society.

native horseradish peroxidase (HRP) enzyme. Chitosan-functionalized Au nanoparticles were heteroaggregated via electrostatic attraction with exfoliated montmorillonite nanoplates by simple mixing followed by sonication to give chitosan-Au/clay composite [115]. The positively charged chitosan-Au was prepared using the $HAuCl_4$ precursor while negatively charged commercial montmorillonite was exfoliated by dispersing the clay in water with ultrasonication. Then, a glass carbon electrode (GCE) was coated with five layers of chitosan-Au/clay, where the native enzyme is intercalated between clay layers. The immobilized HRP showed two quasi-reversible redox peaks at −0.195 V and the biosensor showed a rapid amperometric response to $H_2O_2$ with a wide linear range of 39 μM - 3.1 mM and a detection limit of 9.0 μM. The charge transfer coefficient, electron transfer rate constant, and Michaelis-Menten constant were evaluated to be 0.53, 2.95 $s^{-1}$ and 23.15 mM, respectively.

Alsharif et al. prepared a composite of multi-enzymatic activity consisting of oppositely charged commercial amidine latex (AL) particles and Prussian blue ($Fe^{III}_4[Fe^{II}(CN)_6]_3$) nanoparticles (PB NPs) [30]. The latter was prepared via the co-precipitation of $K_3[Fe(CN)_6]$ and $FeCl_2$. The electrostatic attraction between the negatively charged PB and the positively charged AL enabled to the formation of AL-PB composite. Aqueous dispersions of AL particles and PB NPs were mixed under magnetic stirring. The HRP and superoxide dismutase (SOD) activity of PB NPs was maintained upon immobilization onto AL surface. Fig. 28 shows SEM and TEM images of the AL-PB composite at different amounts of PB. The composite underwent an overall charge reversal as more negatively charged PB NPs were added to positively charged latex. At high and low doses, the composite was highly negatively and positively charged, respectively, and was thus colloidally stable. Around the IEP, however, charges were balanced, and the aggregation is facilitated. The developed hybrid has proven to be an efficient antioxidant of high functional and colloidal stability.

Soh et al. reported a composite of HRP/single-layer titanate ($TiO_x$)/magnetic beads [116]. Single titanate layers were formed by hydrolysis of titanium (IV) tetraisopropoxide liquid with the tetrabutyl ammonium hydroxide solution. The excess salts in the resultant colloid were removed via dialysis with centrifugal filtration. The HRP enzyme as well as the amino-functionalized magnetic beads were obtained commercially. The nanocomposite was formed by mixing the $TiO_x$, HRP and the magnetic particles in slightly acidic solutions and the excess HRP was removed by centrifugation or magnetic separation. The HRP was intercalated into titanate nanosheet, and the composite is formed due to electrostatic interaction between the negatively charged titanate and positively charged magnetic beads and HRP. The immobilized HRP maintained enzymatic activity with *o*-phenylenediamine (OPD), guaiacol, and pyrogallol substrates. The complex was magnetically recoverable, enabling several cycles of use, with a residual activity of 80% after 5 cycles.

Gunawan and Xu developed hollow material by heteroaggregation of anisotropic LDH nanocrystals on carbon nanospheres (CNs) for drug release (Fig. 29) [117]. The LDH was synthesized in pure methanol solvent using mixed solution containing $Mg(NO_3)_2{\cdot}6H_2O$ and $Al(NO_3)_3{\cdot}9H_2O$ while CNs was prepared through carbonization of glucose under hydrothermal conditions. The LDH-CNs hybrid was prepared by

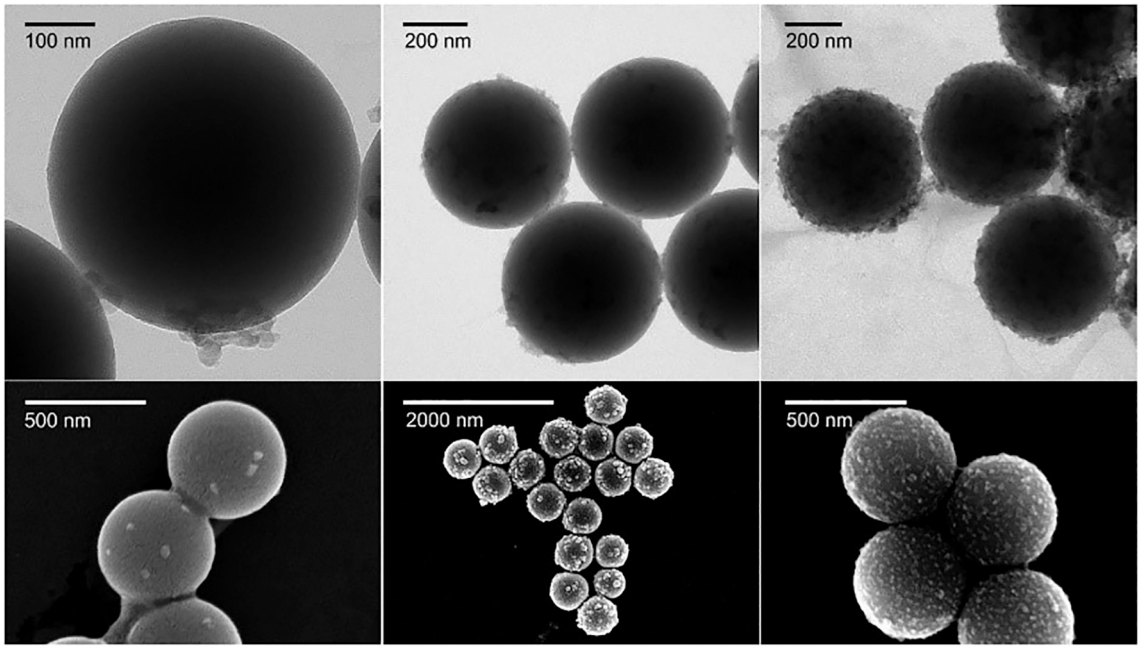


**Fig. 28.** TEM (upper) and SEM (lower) images of the AL-PB composite at 1 (left), 30, (middle), and 600 mg PB/g AL (right) [30]. Reproduced with permission from (Alsharif, N. B.; Samu, G. F.; Sáringer, S.; Muráth, S.; Szilagyi, I., A colloid approach to decorate latex particles with Prussian blue nanozymes. *J. Mol. Liq.* 2020, 309, 113,066). Copyright (2021), with permission from Elsevier. (For interpretation of the references to colour in this figure legend, the reader is referred to the web version of this article.)

mixing methanol-based dispersions of LDH and CNs. The obtained solid phase was calcined to remove the CNs core to give hollow MgAl oxides nanospheres, which were then used for in vitro drug release of ibuprofen. The hollow spheres had good structural integrity and were preserved during the transformation from LDH to oxide, even with a large volume contraction, which is attributed to the densely packed pristine LDH on CNs. Release profiles indicated no significant difference in ibuprofen release between hollow spheres and nanoplates, but hollow nanospheres exhibited lower density, less tendency towards aggregation, higher surface area compared to ibuprofen-LDH nanoplates, which can be utilized to encapsulate other molecules.

A biomedical nanocomposite of manganese ferrite nanoparticles (MFNPs) and oleylamine (OAM)-grafted GO (GO-g-OAM) was prepared by Peng et al. [118]. MFNPs were synthesized via thermolysis whereas GO was prepared through modified Hummer's method. The MFNPs/GO-g-OAM composites (MGONCs) were prepared via mini-emulsion process coupled with solvent evaporation, where $CH_3Cl$-based dispersions of GO-g-OAM and MFNPs were mixed, and the organic solvent was later evaporated. The MGONCs were further functionalized with polyethylene glycol (PEG) functional groups. The loading and size of composites were tailored by altering the GO/MFNPs ratio as well as sonication time. The obtained PEGylated MGONCs showed excellent colloidal stability and biocompatibility as well as excellent performance for hyperthermia and as MRI $T_2$ contrast agents. For 14 nm MFNPs, a specific absorption rate of 1588.83 W/g and a $T_2$ relaxivity value 256.2 $(mM\ Fe)^{-1}\ s^{-1}$ were obtained. Such hydrophobic NPs/GO nanocomposites have high potential for various biomedical applications.

### 4.8. Electrochemical applications

Han et al. prepared a promising electrode material for supercapacitors based on NiAl-LDH and GO quantum dots (GOQDs) [119]. Homogenized formamide-based dispersions of NiAl-LDH sheets and GOQDs were mixed in 1:1, 3:1, 6:1, 9:1 volume ratios to give the GOQDs@NiAl-LDH composites. The NiAl-LDH was prepared by co-precipitation and then delaminated by ultrasonication, while GOQDs were prepared via ball milling. The GOQDs@NiAl-LDH composites showed high specific capacitance, good current charge/discharge characteristics, and high cycle stability. The highest capacitance was obtained when the GOQDs content was 10%. Cyclic voltammetry curves indicated that the energy storage occurred by pseudocapacitance, and electrochemical impedance spectroscopy showed that the impedance of the composite decreased with increasing GOQDs content. The storage capacity of the composite was enabled due to enhanced conductivity and dispersity of NiAl-LDH by GOQDs, which also prevented NiAl-LDH from restacking.

Bai et al. fabricated a functional material for photoanodes for high-efficiency dye-sensitized solar cells, which attract considerable attention worldwide [120]. The nanohybrid is formed via heteroaggregation of exfoliated titania ($Ti_{0.91}O_2$) nanosheets and anatase $TiO_2$ nanoparticles in an aqueous dispersion. $Ti_{0.91}O_2$ nanosheets and $TiO_2$ nanoparticles were prepared by Sasaki's method and hydrolysis, respectively. The electrode is formed by depositing nanohybrid on fluoride-doped tin oxide (FTO) substrate by doctor-blade method. The nanohybrid possesses high light-harvesting efficiency as well as mesoporous structure with slit-shaped pores and large surface area that enables high dye loading. The nanohybrid-based photoanode, illustrated in Fig. 30, demonstrated a higher overall conversion efficiency of 10.1% as well as low charge recombination.

Kim et al. fabricated functional composites with a promising performance as a Si anode material in Li-ion batteries [121]. Commercial Si nanoparticles were incorporated with TEMPO-oxidized cellulose nanofibers (TOCNF) that served as Si nanoparticles reinforcement as well as assistant additive to sodium carboxymethyl cellulose (CMC), which served as the Si anode binder. By mixing an aqueous suspension of TOCNF with Si nanoparticles dispersed in ethanol/water mixture, the Si-TOCNF composite was heteroaggregated and later retrieved via freeze-drying. The Si electrode was prepared by casting a slurry mixture containing the Si-TOCNF sample, conductive additive, and CMC binder with different weight ratios on a Cu foil with a doctor blade and dried in a vacuum oven. The effective interaction between TOCNF and Si nanoparticles was attributed to the hydrogen bonding, induced by the carboxylic groups of TOCNF. As a reinforcement fiber, the one-dimensional nature of TOCNF enhanced the mechanical properties such as hardness

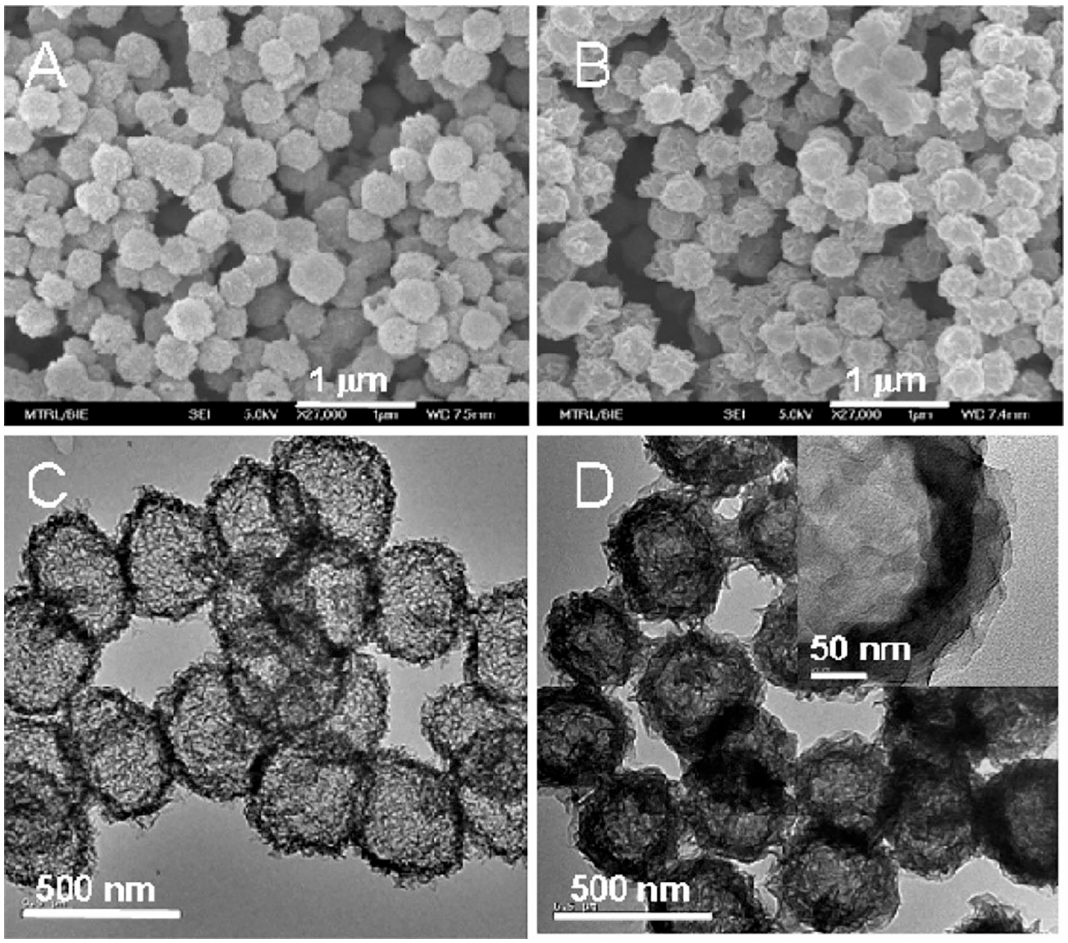


**Fig. 29.** (A) SEM and (C) TEM images of hollow MgAl oxide nanospheres obtained after calcination of LDH/CNs. (B) SEM and (D) TEM images of ibuprofen intercalated LDH hollow nanospheres after reconstruction [117]. Reprinted (adapted) with permission from (Gunawan, P.; Xu, R., Direct assembly of anisotropic layered double hydroxide (LDH) nanocrystals on spherical template for fabrication of drug-LDH hollow nanospheres. *Chem. Mat.* 2009, 21 (5), 781–783). Copyright (2021) American Chemical Society.

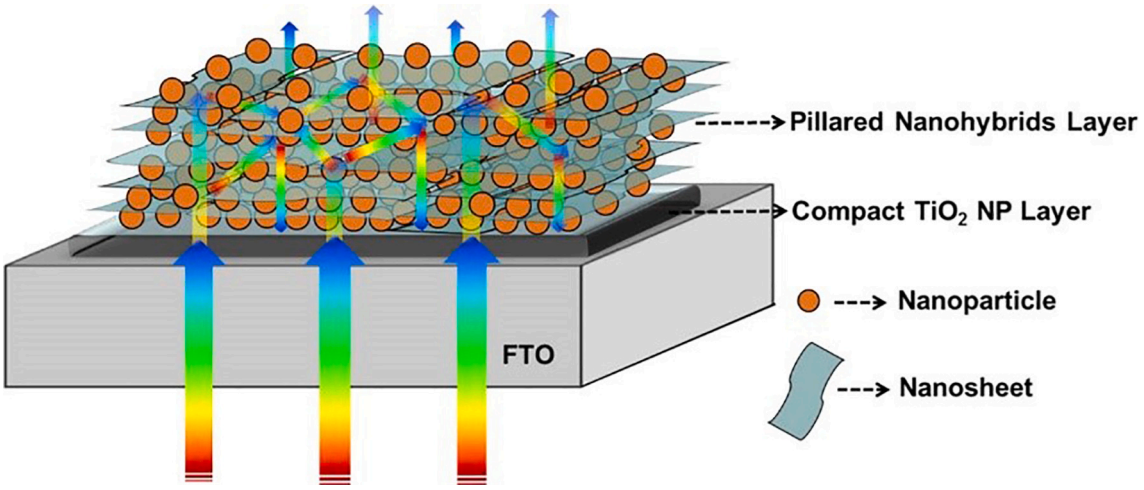


**Fig. 30.** Schematic diagram of layered nanohybrid-based photoanodes for solar cells [120]. Reprinted (adapted) with permission from (Bai, Y.; Xing, Z.; Yu, H.; Li, Z.; Amal, R.; Wang, L. Z., Porous Titania Nanosheet/Nanoparticle Hybrids as Photoanodes for Dye-Sensitized Solar Cells. *ACS Appl. Mater. Interfaces,* 2013, 5 (22), 12,058–12,065). Copyright (2021) American Chemical Society.

and reduced elastic modulus, better stress dissipation, and structural integrity to the Si electrode. TOCNF additive also significantly improved the CMC binder uniformity, which result in a better protected electrode surface.

### 4.9. Sensor development

Wang et al. fabricated an HRP/CDs/LDH composite for hydrogen peroxide biosensing [122]. The highly pure CoFe-LDH platelets were

synthesized via co-precipitation, whereas carbon nanodots (CDs) were prepared by hydrothermal treatment. The HRP/CDs/LDH composite was prepared by mixing suspensions of CoFe-LDH and CDs followed by the addition of HRP suspension into the CDs/LDH mixture. The resulting suspension was cast on the pre-treated GCE surface. Cyclic voltammogram shows changes in the anodic and cathodic peak currents indicating an excellent electrocatalytic activity towards $H_2O_2$. Also, no significant changes in the current response were observed even when the concentrations of the interfering substances such as epinephrine, uric acid, and ascorbic acid were 10 times that of the $H_2O_2$. The biosensor maintained 87.6% of its original current response after one week of storage. Such outstanding properties of the HRP/CDs/LDH-based biosensor are attributed to the synergistic effect among the three constituents.

Amjadi et al. assembled a fluorescent probe for the detection of uric acid with satisfactory results upon analysis of human plasma and urine. The probe is based on a nanocomposite of nitrogen/sulfur co-doped carbon dots (S/N-CDs) and $MnO_2$ nanosheets, which have rich redox chemistry and high extinction coefficient [123]. The S/N-CDs were synthesized via the hydrothermal method using citric acid and L-cysteine, while $MnO_2$ nanosheets were prepared using $MnCl_2{\cdot}4H_2O$ salt. The fluorescent composite S/N-CDs-$MnO_2$ was prepared by mixing aqueous dispersions of $MnO_2$ and S/N-CDs in the presence of Britton-Robinson buffer. The addition of $MnO_2$ nanosheets quenches the fluorescence due to the inner filter effect of the sheets; however, the addition of uric acid to the S/N-CDs-$MnO_2$ composite restores the fluorescence due to interaction with the $MnO_2$ nanosheets. The low-cost probe showed environmental friendliness, good selectivity, and fast fluorescence response.

Dong et al. developed a fluorescent substrate by heteroaggregation of $MnO_2$ nanosheets and polyethyleneimine-functionalized carbon dots (p-CDs), prepared by reduction and hydrothermal methods, respectively [124]. In the p-CDs@$MnO_2$ composite, $MnO_2$ nanosheets quenches the fluorescence of p-CDs via Förster resonance energy transfer, which can be restored by the addition of ascorbic acid due to reduction of $Mn^{4+}$ in $MnO_2$ to $Mn^{2+}$. Ascorbic acid is produced by hydrolysis of 2-phosphoascorbic acid by alkaline phosphatase, and thus the p-CDs@$MnO_2$ composite was used as the fluorescence probe in a developed fluorescence enzyme-linked immunosorbent assay (ELISA), which showed good accuracy, precision, and high specificity for the detection of amantadine. In chicken meat tissues, samples with amantadine concentrations as low as 0.6, 3.0 and 10.0 ng/mL were detected by fluorescent ELISA, making it a great candidate to be applied in detecting trace chemical contaminants in food.

In another work by He et al., a novel composite of nitrogen-doped quantum dot (CQDs) and the $MnO_2$ nanosheets was developed as a turn-on fluorescence probe for detection of glutathione, as shown in Fig. 31. In the $MnO_2$-CQDs nanocomposite, $MnO_2$ nanosheets were fluorescence quenchers, due to reduction of $Mn^{4+}$ to $Mn^{2+}$, while CQDs served as fluorescence reporter. The oppositely charged CQDs and $MnO_2$ nanosheets formed through electrostatic interaction. The low-cost composite showed excellent biocompatibility, high selectivity, and sensitivity with a detection limit of 10 nM glutathione, and thus it was used to detect glutathione level in living cells [125].

### 4.10. Ceramics

Ceramic composites are very versatile materials with excellent physicochemical properties compared to their single-phase counterparts. The combination of matrix and reinforcement components have led to significant improvements in various properties such as thermal conductivity, mechanical strength, and hardness [126]. Among preparation strategies of these composites is heteroaggregation, where the components are mixed and homogenized before subjected to consolidation, a thermal treatment process such as sintering and hot pressing.

Madhavan et al. prepared porous ceramics from a Pickering emulsion of oppositely charged silica and alumina particles dispersed in decane/water mixture [127]. Equal volumes of decane and 1% (w/w) aqueous suspension of both particles are mixed and homogenized mechanically. The high stability of the emulsion is attributed to the electrostatic heteroaggregation between silica and alumina particles, and the subsequent adsorption of silica-alumina aggregates to the oil-water interface. By tuning the experimental conditions, gel-like Pickering emulsions serve as excellent templates for the fabrication of porous ceramics. By emulsion drying and sintering, the porous mullite ceramic structure had exceptional thermal and chemical resistance under harsh conditions.

In addition, Muñoz et al. utilized electrostatic heteroaggregation of

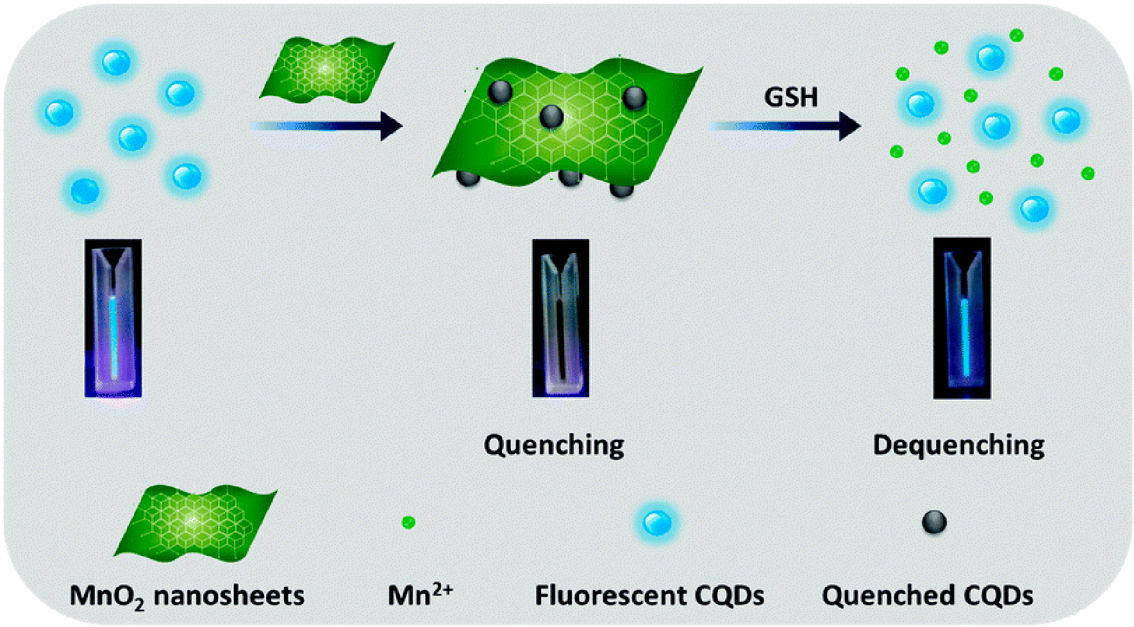


**Fig. 31.** The glutathione sensing mechanism through turn-on fluorescence using fluorescent CQDs quenched by $MnO_2$ nanosheets [125]. Reproduced from (He, D. G.; Yang, X. X.; He, X. X.; Wang, K. M.; Yang, X.; He, X.; Zou, Z., A sensitive turn-on fluorescent probe for intracellular imaging of glutathione using single-layer $MnO_2$ nanosheet-quenched fluorescent carbon quantum dots. *Chem. Commun.* 2015, 51 (79), 14,764–14,767) with permission from The Royal Society of Chemistry.

commercial and oppositely charged $Al_2O_3$ platelets as well as silica and α-$Al_2O_3$ nanoparticles [128]. After mixing the relevant aqueous suspensions, the resulting three-component heteroaggregates were shaped into solid pellets via sedimentation and freeze-granulation methods. The solid pellets were obtained by drying and were later thermally treated using field assisted sintering to obtain nacre-like ceramic composites. Both shaping methods resulted in good component distribution as well as good alignment of alumina platelets in the sintered samples. The composite obtained by sedimentation had better flexural strength. However, samples obtained by freeze-casting had better mechanical properties despite a better alignment of platelets in sedimentation-prepared pellets as a result of the difference in the vitreous phase composition.

Fan et al. prepared several ceramic composites of multi-walled CNTs and alumina particles to probe the mechanical and electrical properties at different preparation conditions [129]. The CNTs/$Al_2O_3$ composites were heteroaggregated by mixing separate aqueous suspensions of CNTs and $Al_2O_3$ in the absence and presence of dispersants (SDS and AG). The resulting slurries were ball milled for a prolonged period of time and dried. The obtained solids were consolidated by hot pressing with uniaxial pressure under argon atmosphere to obtain ceramic CNTs/$Al_2O_3$ composites. Compared to pure $Al_2O_3$, the SDS-dispersed CNTs resulted in 1.8 times increase in fracture toughness of ceramic CNTs/$Al_2O_3$ composites that are 4% (w/w) in CNTs. When the CNTs and $Al_2O_3$ were dispersed with SDS and AG, respectively, the resulting ceramics composite (2% (w/w) CNTs/$Al_2O_3$) had 1.3 increase in fracture toughness and 14 orders of magnitude decrease in resistivity, compared to pure $Al_2O_3$.

Kaźmierczak-Bałata and Mazur probed the effect of carbon nanoparticles (graphene and GO) reinforcement on the mechanical and thermal properties of SiC ceramics, using different forms of commercially available SiC [130]. The SiC-carbon ceramic composites were prepared by first mixing the SiC power with an aqueous suspension of the relevant carbon nanoparticles that contain sintering additives (boron power and glucose). The resulting suspension was then heated until complete water evaporation, and the obtained sample was then thermally treated using the spark plasma sintering process to obtain ceramic composites. Incorporation of 2.5% (w/w) GO enhanced both the mechanical and thermal properties of the resulting composite, although it caused a slight decrease in the density. Besides, graphene had no effect on the mechanical and thermal properties. With GO reinforcement, the composite toughness as well as the thermal diffusivity increased from 1.21 to 1.75 $MPa/m^{1/2}$ and from 0.60 to 0.71 $cm^2/s$, respectively, while the friction coefficient changed from 0.62 to 0.66. Thermal imaging revealed homogeneity of the local thermal properties of the products fabricated from the starting SiC powder.

## 5. Summary and outlook

The heteroaggregation process is a fundamental and complex phenomenon in multi-component colloidal systems and has been significantly explored both theoretically and experimentally. Such systems occur widely in nature as well as in numerous industrial applications. As seen before, the kinetics of heteroaggregation is heavily dependent on many factors such as the chemical composition, the particle size, the solvent, the pH, particle concentration, ionic strength, the surface charge, the presence of surface-active compounds, etc. By careful interplay of these factors, highly functional novel nanostructured composites have been prepared and utilized in several fields such as drug delivery, energy, catalysis, enzyme mimicking, etc.

Despite these successes, there has been no comprehensive view that completely explains the heteroaggregation process, and a full theoretical understanding still does not exist owing to the nature and the complexity of the phenomenon. Moreover, the extension of the DLVO theory to encompass heteroaggregation has also resulted in discrepancies between theoretical predictions and experimental findings, which can be attributed to the numerous assumptions such as smoothness of the surface, constant charge, and potential as well as the negligence of particle-particle interactions. In addition, numerous experimental conditions such as non-aqueous media resulted in several non-DLVO type forces such as short-range attraction, depletion effect, hydrophobic interaction, and acid-base interactions, which could not be explained by the DLVO theory.

Finally, the heteroaggregation field in colloidal systems is still in its infancy owing to the numerous complications and involved variables, and a thorough understanding of the process and occurring interactions remains an unmet challenge with extensive work yet to be done. It is hoped that the present review helps to gain insight into the heteroaggregation processes and assists in designing more experiments to further improve our understanding in the colloidal domain.

## List of abbreviations

| | |
|---|---|
| DLVO | Boris Derjaguin, Lev Landau, Evert Verwey and Theodoor Overbeek |
| SEM | Scanning electron microscopy |
| TEM | Transmission electron microscopy |
| HRTEM | High resolution transmission electron microscopy |
| HR-SEM | High resolution scanning electron microscopy |
| FE-SEM | Field emission scanning electron microscopy |
| cryo-FEGSEM | Cryogenic field emission gun scanning electron microscopy |
| cryo-TEM | Cryogenic transmission electron microscopy |
| EDX | Energy-dispersive X-ray spectroscopy |
| nZVI | Zero-valence iron nanoparticles |
| CMP | Clay mineral particles |
| POM | Particulate organic matter |
| PCM | Pyrogenic carbonaceous material |
| KGA | Kaolinite and goethite associations |
| GO | Graphene oxide |
| LDH | Layered double hydroxides |
| PDADMAC | Poly(diallyldimethylammonium chloride) |
| PNIPAM | Poly(N-isopropylacrylamide) |
| MMA | Methyl methacrylate |
| BA | Butyl acrylate |
| PBMA | Poly(butyl methacrylate) |
| HMPS | Sodium 2-hydroxyl-3-(methacryloxy)propane-1-sulfonate |
| SDS | Sodium dodecyl sulfate |
| CTAB | Cetrimonium bromide |
| CTA | Cetyltrimethyl ammonium |
| HA | Humic acid |
| OA | Octylamine |
| PTFE | Polytetrafluoroethylene |
| IEP | Isoelectric point |
| CCC | Critical coagulation concentration |
| LBL | Layer-by-layer assembly |
| PS | Polystyrene latex |
| CNTs | Carbon nanotubes |
| TBARs | Thiobarbituric acid reactive substances |
| VB9 | Vitamin B9 |
| NMP | *N*-methyl-2-pyrrolidone |
| Reduced GO | rGO |
| MB | Methylene blue |
| NCs | Nanoclusters/Nanocubes |
| LDO | Layered double oxides |
| CSs | Carbon spheres |
| CNs | Carbon nanospheres |
| PVP | Poly(vinyl pyrrolidone) |
| THF | Tetrahydrofuran |
| SERS | Surface enhanced Raman scattering |
| ROS | Reactive oxygen species |
| TMB | 3,3′,5,5′-tetramethylbenzidine |
| ABTS | 2,2′-azino-bis(3-ethylbenzthiazoline-6-sulphonic acid) |
| OPD | O-phenylenediamine |
| HUVEC | Human umbilical vein endothelial cells |
| CHO | Chinese hamster ovary cells |
| MRI | Magnetic resonance imaging |
| HRP | Horseradish peroxidase |
| GCE | Glass carbon electrode |
| AL | Amidine latex |
| PB | Prussian blue |
| HemNP | Hematite nanoparticles |

(*continued on next page*)

(*continued*)

| | |
|---|---|
| SOD | Superoxide dismutase |
| DPPH | 2,2-diphenyl-1-picrylhydrazyl |
| OAM | Oleylamine |
| PEG | Polyethylene glycol |
| PAA | Polyacrylic acid |
| GOQDs | Graphene oxide quantum dots |
| FTO | Fluoride-doped tin oxide |
| CDs | Carbon nanodots |
| ELISA | Enzyme linked immunosorbent assay |
| p-CDs | Polyethyleneimine-functionalized carbon dots |
| S/N-CDs | Nitrogen/sulfur co-doped carbon dots |
| CQDs | Nitrogen-doped quantum dots |
| AB | Lewis acid-base |
| NPs | Nanoparticles |
| MFNPs | Manganese ferrite nanoparticles |
| UV | Ultraviolet |
| AG | Arabic gum |
| NFC | Nanofibrillated cellulose |
| CNF | Cellulose nanofibers |
| BCNF | Bacterial cellulose nanofibers |
| TEMPO | 2,2,6,6-Tetramethyl-1-piperidine oxyl |
| TOCNF | TEMPO-oxidized cellulose nanofibers |
| CHNF | Chitosan nanofibers |
| BT | Barium titanate |
| APO | Apoferritin |
| BLG | β-lactoglobulin |
| CMC | Carboxymethyl cellulose |

## Declaration of Competing Interest

The authors declare that they have no known competing financial interests or personal relationships that could have appeared to influence the work reported in this paper.

## Acknowledgment

Financial support from the Ministry of Human Capacities (20391-3/2018/FEKUSTRAT) and the Hungarian Academy of Sciences/Eötvös Lóránd Research Network (96130) is gratefully acknowledged. The support from the University of Szeged Open Access Fund (5267) is gratefully acknowledged.

## References

[1] Dickinson E. Food colloids research: historical perspective and outlook. Adv Colloid Interface Sci 2011;165:7–13.
[2] Feng LL, Stuart MC, Adachi Y. Dynamics of polyelectrolyte adsorption and colloidal flocculation upon mixing studied using mono-dispersed polystyrene latex particles. Adv Colloid Interface Sci 2015;226:101–14.
[3] Moore TL, Rodriguez-Lorenzo L, Hirsch V, Balog S, Urban D, Jud C, et al. Nanoparticle colloidal stability in cell culture media and impact on cellular interactions. Chem Soc Rev 2015;44:6287–305.
[4] Pavlovic M, Rouster P, Oncsik T, Szilagyi I. Tuning colloidal stability of layered double hydroxides: from monovalent ions to polyelectrolytes. ChemPlusChem 2017;82:121–31.
[5] Muráth S, Sáringer S, Somosi Z, Szilagyi I. Effect of ionic compounds of different valences on the stability of titanium oxide colloids. Coll Interf 2018;2:32.
[6] Shrestha S, Wang B, Dutta P. Nanoparticle processing: understanding and controlling aggregation. Adv Colloid Interface Sci 2020;279:102162.
[7] Dickinson E. Structuring of colloidal particles at interfaces and the relationship to food emulsion and foam stability. J Colloid Interface Sci 2015;449:38–45.
[8] Santos AC, Ferreira C, Veiga F, Ribeiro AJ, Panchal A, Lvov Y, et al. Halloysite clay nanotubes for life sciences applications: from drug encapsulation to bioscaffold. Adv Colloid Interface Sci 2018;257:58–70.
[9] Cao ZB, Li B, Sun LY, Li L, Xu ZP, Gu Z. 2D layered double hydroxide nanoparticles: recent progress toward preclinical/clinical nanomedicine. Small Methods 2019;4:1900343.
[10] Bolto B, Gregory J. Organic polyelectrolytes in water treatment. Water Res 2007;41:2301–24.
[11] Martinez-Pedrero F, Alousque F, de Gaudemaris B, Berriot J, Gaboriaud F, Bremond N, et al. Making an elastomeric composite material via the heteroaggregation of a binary colloidal dispersion. Soft Matter 2012;8:8752–7.
[12] Thomas AW, Foster SB. The colloid content of vegetable tanning extracts. J Ind Eng Chem 1922;14:191–5.
[13] Farrokhpay S. A review of polymeric dispersant stabilisation of titania pigment. Adv Colloid Interface Sci 2009;151:24–32.
[14] Hubbe MA, Nanko H, McNeal MR. Retention aid polymer interactions with cellulosic surfaces and suspensions: a review. BioResources 2009;4:850–906.
[15] Yu WL, Borkovec M. Distinguishing heteroaggregation from homoaggregation in mixed binary particle suspensions by multiangle static and dynamic light scattering. J Phys Chem B 2002;106:13106–10.
[16] Lopez-Lopez JM, Schmitt A, Moncho-Jorda A, Hidalgo-Alvarez R. Electrostatic heteroaggregation regimes in colloidal suspensions. Adv Colloid Interface Sci 2009;147:186–204.
[17] Cao TC, Borkovec M, Trefalt G. Heteroaggregation and homoaggregation of latex particles in the presence of alkyl sulfate surfactants. Coll Interf 2020;4:52.
[18] Wang HT, Adeleye AS, Huang YX, Li FT, Keller AA. Heteroaggregation of nanoparticles with biocolloids and geocolloids. Adv Colloid Interface Sci 2015;226:24–36.
[19] Buffle J, Wilkinson KJ, Stoll S, Filella M, Zhang JW. A generalized description of aquatic colloidal interactions: the three-colloidal component approach. Environ Sci Technol 1998;32:2887–99.
[20] Jiang CL, Sequaris JM, Vereecken H, Klumpp E. Effects of inorganic and organic anions on the stability of illite and quartz soil colloids in Na-, Ca- and mixed Na-Ca systems. Colloid Surf A 2012;415:134–41.
[21] Chanudet V, Filella M. The fate of inorganic colloidal particles in Lake Brienz. Aquat Sci 2007;69:199–211.
[22] Missana T, Adell A. On the applicability of DLVO theory to the prediction of clay colloids stability. J Colloid Interface Sci 2000;230:150–6.
[23] Oriekhova O, Stoll S. Heteroaggregation of nanoplastic particles in the presence of inorganic colloids and natural organic matter. Environ Sci Nano 2018;5:792–9.
[24] Moore PS. Deltaic sedimentation. Earth Sci Rev 1966;1:87–104.
[25] Xing YW, Xu MD, Gui XH, Cao YJ, Rudolph M, Butt HJ, et al. The role of surface forces in mineral flotation. Curr Opin Colloid Interface Sci 2019;44:143–52.
[26] Dabros T, Vandeven TGM. Kinetics of coating by colloidal particles. J Colloid Interface Sci 1982;89:232–44.
[27] Zubair M, Daud M, McKay G, Shehzad F, Al-Harthi MA. Recent progress in layered double hydroxides (LDH)-containing hybrids as adsorbents for water remediation. Appl Clay Sci 2017;143:279–92.
[28] Wang J, Xu F, Jin HY, Chen YQ, Wang Y. Non-noble metal-based carbon composites in hydrogen evolution reaction: fundamentals to applications. Adv Mater 2017;29:1605838.
[29] Siedl N, Baumann SO, Elser MJ, Diwald O. Particle networks from powder mixtures: generation of $TiO_2$-$SnO_2$ heterojunctions via surface charge-induced heteroaggregation. J Phys Chem C 2012;116:22967–73.
[30] Alsharif NB, Samu GF, Sáringer S, Muráth S, Szilagyi I. A colloid approach to decorate latex particles with Prussian blue nanozymes. J Mol Liq 2020;309:113066.
[31] Patil AJ, Mann S. Self-assembly of bio-inorganic nanohybrids using organoclay building blocks. J Mater Chem 2008;18:4605–15.
[32] Losch P, Huang WX, Goodman ED, Wrasman CJ, Holm A, Riscoe AR, et al. Colloidal nanocrystals for heterogeneous catalysis. Nano Today 2019;24:15–47.
[33] Zhao Y, Zhao M, Ding X, Liu ZR, Tian H, Shen HH, et al. One-step colloid fabrication of nickel phosphides nanoplate/nickel foam hybrid electrode for high-performance asymmetric supercapacitors. Chem Eng J 2019;373:1132–43.
[34] Guo C, Zhang Y, Yin M, Shi J, Zhang W, Wang X, et al. $Co_3O_4$@$Co_3S_4$ core-shell neuroid network for high cycle-stability hybrid-supercapacitors. J Power Sources 2021;485:229315.
[35] Zhai YC, Shen FZ, Zhang XT, Jing PT, Li D, Yang XD, et al. Synthesis of green emissive carbon dots@montmorillonite composites and their application for fabrication of light-emitting diodes and latent fingerprints markers. J Colloid Interface Sci 2019;554:344–52.
[36] Bharadwaj S, Pandey A, Yagci B, Ozguz V, Qureshi A. Graphene nano-mesh-Ag-ZnO hybrid paper for sensitive SERS sensing and self-cleaning of organic pollutants. Chem Eng J 2018;336:445–55.
[37] Yan LK, Zhang G, Zhang L, Zhang W, Gu JC, Huang YJ, et al. Robust construction of underwater superoleophobic CNTs/nanoparticles multifunctional hybrid membranes via interception effect for oily wastewater purification. J Membr Sci 2019;569:32–40.
[38] Hernandez-Montelongo J, Fernandez-Fierro C, Benito-Gomez N, Romero-Saez M, Parodi J, Carmona ER, et al. Hybrid porous silicon/green synthetized Ag microparticles as potential carries for Ag nanoparticles and drug delivery. Mater Sci Eng C Mater Biol Appl 2020;116:111183.
[39] Ding Q, Liu DF, Guo DW, Yang F, Pang XY, Che BRE, et al. Shape-controlled fabrication of magnetite silver hybrid nanoparticles with high performance magnetic hyperthermia. Biomaterials 2017;124:35–46.
[40] Li P, Guo W, Lu Z, Tian J, Li X, Wang H. UV-responsive single-microcapsule self-healing material with enhanced UV-shielding $SiO_2$/ZnO hybrid shell for potential application in space coatings. Prog Org Coat 2021;151:106046.
[41] Derjaguin B, Landau LD. Theory of the stability of strongly charged lyophobic sols and of the adhesion of strongly charged particles in solutions of electrolytes. Acta Phys Chim 1941;14:633–62.
[42] Verwey EJW, Overbeek JTG. Theory of stability of lyophobic colloids. Amsterdam: Elsevier; 1948.
[43] Israelachvili J. Intermolecular and surface forces. 3rd ed. London: Academic Press; 2011.
[44] Wang YL, Yang K, Chefetz B, Xing BS, Lin DH. The pH and concentration dependent interfacial interaction and heteroaggregation between nanoparticulate zero-valent iron and clay mineral particles. Environ Sci Nano 2019;6:2129–40.

[45] Jiang LH, Liu YG, Zeng GM, Liu SB, Que W, Li J, et al. Adsorption of 17 beta-estradiol by graphene oxide: effect of heteroaggregation with inorganic nanoparticles. Chem Eng J 2018;343:371–8.
[46] Ben Moussa O, Tinat L, Jin XJ, Baaziz W, Durupthy O, Sayag C, et al. Heteroaggregation and selective deposition for the fine design of nanoarchitectured bifunctional catalysts: application to hydroisomerization. ACS Catal 2018;8:6071–8.
[47] Luo MX, Qi XJ, Ren TX, Huang YX, Keller AA, Wang HT, et al. Heteroaggregation of $CeO_2$ and $TiO_2$ engineered nanoparticles in the aqueous phase: application of turbiscan stability index and fluorescence excitation-emission matrix (EEM) spectra. Colloid Surf A Physicochem Eng Asp 2017;533:9–19.
[48] Zhao J, Liu FF, Wang ZY, Cao XS, Xing BS. Heteroaggregation of graphene oxide with minerals in aqueous phase. Environ Sci Technol 2015;49:2849–57.
[49] Lopez-Lopez JM, Schmitt A, Moncho-Jorda A, Hidalgo-Alvarez R. Stability of binary colloids: kinetic and structural aspects of heteroaggregation processes. Soft Matter 2006;2:1025–42.
[50] Dusak P, Mertelj A, Kralj S, Makovec D. Controlled heteroaggregation of two types of nanoparticles in an aqueous suspension. J Colloid Interface Sci 2015;438:235–43.
[51] Cao TC, Sugimoto T, Szilagyi I, Trefalt G, Borkovec M. Heteroaggregation of oppositely charged particles in the presence of multivalent ions. Phys Chem Chem Phys 2017;19:15160–71.
[52] Wang XN, Wang S, Pan XL, Gadd GM. Heteroaggregation of soil particulate organic matter and biogenic selenium nanoparticles for remediation of elemental mercury contamination. Chemosphere 2019;221:486–92.
[53] Hogg R, Healy TW, D.W.. F. Mutual coagulation of colloidal dispersions. Trans Faraday Soc 1966;62:1638–51.
[54] Trefalt G, Montes Ruiz-Cabello FJ, Borkovec M. Interaction forces, heteroaggregation and deposition involving charged colloidal particles. J Phys Chem B 2014;118:6346–55.
[55] Cerbelaud A, Videcoq A, Pagnoux C, Rossignol F, Ferrando R. Heteroaggregation between $Al_2O_3$ submicrometer particles and $SiO_2$ nanoparticles: experiment and simulation. Langmuir 2008;24:3001–8.
[56] Moazzami-Gudarzi M, Adam P, Smith AM, Trefalt G, Szilagyi I, Maroni P, et al. Interactions between similar and dissimilar charged interfaces in the presence of multivalent anions. Phys Chem Chem Phys 2018;20:9436–48.
[57] Trefalt G, Szilagyi I, Oncsik T, Sadeghpour A, Borkovec M. Probing colloidal particle aggregation by light scattering. Chimia 2013;67:772–6.
[58] Voorn DJ, Ming W, Laven J, Meuldijk J, de With G, van Herk AM. Plate-sphere hybrid dispersions: Heterocoagulation kinetics and DLVO evaluation. Colloid Surf A 2007;294:236–46.
[59] Lin W, Kobayashi M, Skarba M, Mu C, Galletto P, Borkovec M. Heteroaggregation in binary mixtures of oppositely charged colloidal particles. Langmuir 2006;22:1038–47.
[60] Bansal P, Deshpande AP, Basavaraj MG. Hetero-aggregation of oppositely charged nanoparticles. J Colloid Interface Sci 2017;492:92–100.
[61] Parsai T, Kumar A. Understanding effect of solution chemistry on heteroaggregation of zinc oxide and copper oxide nanoparticles. Chemosphere 2019;235:457–69.
[62] Nakamura Y, Okachi M, Toyotama A, Okuzono T, Yamanaka J. Controlled clustering in binary charged colloids by adsorption of ionic surfactants. Langmuir 2015;31:13303–11.
[63] Lu XY, Lu TT, Zhang HJ, Shang ZB, Chen JY, Wang Y, et al. Effects of solution chemistry on the attachment of graphene oxide onto clay minerals. Environ Sci Process Impacts 2019;21:506–13.
[64] Harley S, Thompson DW, Vincent B. The adsorption of small particles onto larger particles of opposite charge. Direct electron microscope studies. Colloids Surf 1992;62:163–76.
[65] Yu WL, Matijevic E, Borkovec M. Absolute heteroaggregation rate constants by multiangle static and dynamic light scattering. Langmuir 2002;18:7853–60.
[66] Singh N, Tiwari E, Khandelwal N, Darbha GK. Understanding the stability of nanoplastics in aqueous environments: effect of ionic strength, temperature, dissolved organic matter, clay, and heavy metals. Environ Sci Nano 2019;6:2968–76.
[67] Barton LE, Therezien M, Auffan M, Bottero JY, Wiesner MR. Theory and methodology for determining nanoparticle affinity for heteroaggregation in environmental matrices using batch measurements. Environ Eng Sci 2014;31:421–7.
[68] Tombacz E, Csanaky C, Illes E. Polydisperse fractal aggregate formation in clay mineral and iron oxide suspensions, pH and ionic strength dependence. Colloid Polym Sci 2001;279:484–92.
[69] Guo BL, Jiang JC, Serem W, Sharma VK, Ma XM. Attachment of cerium oxide nanoparticles of different surface charges to kaolinite: molecular and atomic mechanisms. Environ Res 2019;177:108645.
[70] Khalil AM, Hassan ML, Ward AA. Novel nanofibrillated cellulose/polyvinylpyrrolidone/silver nanoparticles films with electrical conductivity properties. Carbohydr Polym 2017;157:503–11.
[71] Hassan ML, Ali AF, Salama AH, Abdel-Karim AM. Novel cellulose nanofibers/barium titanate nanoparticles nanocomposites and their electrical properties. J Phys Org Chem 2019;32:3897.
[72] Huynh KA, McCaffery JM, Chen KL. Heteroaggregation of multiwalled carbon nanotubes and hematite nanoparticles: rates and mechanisms. Environ Sci Technol 2012;46:5912–20.
[73] Jurado R, Galvez N. Apoferritin amyloid-fibril directed the in situ assembly and/or synthesis of optical and magnetic nanoparticles. Nanomaterials 2021;11:146.
[74] Liu X, Xu XT, Sun J, Duan SX, Sun YB, Hayat T, et al. Interaction between $Al_2O_3$ and different sizes of GO in aqueous environment. Environ Pollut 2018;243:1802–9.
[75] Chen B, Sun WL, Wang CH, Guo XY. Size-dependent impact of inorganic nanoparticles on sulfamethoxazole adsorption by carbon nanotubes. Chem Eng J 2017;316:160–70.
[76] de Mendonca VR, Dalmaschio CJ, Leite ER, Niederberger M, Ribeiro C. Heterostructure formation from hydrothermal annealing of preformed nanocrystals. J Mater Chem A 2015;3:2216–25.
[77] Yi P, Pignatello JJ, Uchimiya M, White JC. Heteroaggregation of cerium oxide nanoparticles and nanoparticles of pyrolyzed biomass. Environ Sci Technol 2015;49:13294–303.
[78] Zanini M, Hsu CP, Magrini T, Marini E, Isa L. Fabrication of rough colloids by heteroaggregation. Colloid Surf A Physicochem Eng Asp 2017;532:116–24.
[79] Veschambres C, Halma M, Bourgeat-Lami E, Chazeau L, Dalmas F, Prevot V. Layered double hydroxides: efficient fillers for waterborne nanocomposite films. Appl Clay Sci 2016;130:55–61.
[80] Ji YQ, Black L, Weidler PG, Janek M. Preparation of nanostructured materials by heterocoagulation-interaction of montmorillonite with synthetic hematite particles. Langmuir 2004;20:9796–806.
[81] Voorn DJ, Ming W, van Herk AM, Bomans PHH, Frederik PM, Gasemjit P, et al. Controlled heterocoagulation of platelets and spheres. Langmuir 2005;21:6950–6.
[82] Yang JT, Chen F, Ye YC, Fei ZD, Zhong MQ. Preparation and characterization of polystyrene (PS)/layered double hydroxides (LDHs) composite by a heterocoagulation method. Colloid Polym Sci 2010;288:761–7.
[83] Pavlovic M, Rouster P, Bourgeat-Lami E, Prevot V, Szilagyi I. Design of latex-layered double hydroxide composites by tuning the aggregation in suspensions. Soft Matter 2017;13:842–51.
[84] Li H, Deng L, Zhu G, Kang L, Liu Z-H. Fabrication and capacitance of $Ni^{2+}$–$Fe^{3+}$ LDHs/$MnO_2$ layered nanocomposite via an exfoliation/reassembling process. Mater Sci Eng B 2012;177:8–13.
[85] Nethravathi C, Viswanath B, Shivakumara C, Mahadevaiah N, Rajamathi M. The production of smectite clay/graphene composites through delamination and co-stacking. Carbon 2008;46:1773–81.
[86] Lagaly G, Mecking O, Penner D. Colloidal magnesium aluminum hydroxide and heterocoagulation with a clay mineral. II. Heterocoagulation with sodium montmorillonite. Colloid Polym Sci 2001;279:1097–103.
[87] Huang GX, Guo HY, Zhao J, Liu YH, Xing BS. Effect of co-existing kaolinite and goethite on the aggregation of graphene oxide in the aquatic environment. Water Res 2016;102:313–20.
[88] Jones OG, Handschin S, Adamcik J, Harnau L, Bolisetty S, Mezzenga R. Complexation of b-lactoglobulin fibrils and sulfated polysaccharides. Biomacromolecules 2011;12:3056–65.
[89] Pita IA, Singh S, Silien C, Ryan KM, Liu N. Heteroaggregation assisted wet synthesis of core-shell silver-silica-cadmium selenide nanowires. Nanoscale 2016;8:1200–9.
[90] Yan WJ, Chen WB, Muhammad U, Zhang JH, Zhuang H, Zhou GH. Preparation of alpha-tocopherol-chitosan nanoparticles/chitosan/montmorillonite film and the antioxidant efficiency on sliced dry-cured ham. Food Control 2019;104:132–8.
[91] Mallakpour S, Hatami M. Green and eco-friendly route for the synthesis of Ag@vitamin B9-LDH hybrid and its chitosan nanocomposites: characterization and antibacterial activity. Polymer 2018;154:188–99.
[92] Pricilla RB, Bhuvanesh N, David CI, Murugan S, Nandhakumar R. GO/NiO nanocomposite: Chemosensor for L-Leucine and a potential antibacterial agent. Mater Today Chem 2021. https://doi.org/10.1016/j.matpr.2020.11.466.
[93] Almasi H, Jafarzadeh P, Mehryar L. Fabrication of novel nanohybrids by impregnation of CuO nanoparticles into bacterial cellulose and chitosan nanofibers: characterization, antimicrobial and release properties. Carbohydr Polym 2018;186:273–81.
[94] Li J, Xu Y, Wang S, Zhang H. Ultrafine AuPd nanoclusters on layered double hydroxides by the capt-capped AuPd cluster precursor method: synergistic effect for highly efficient aerobic oxidation of alcohols. J Phys Chem C 2019;123:15483–94.
[95] Li L, Feng YJ, Li YS, Zhao WR, Shi JL. $Fe_3O_4$ core/layered double hydroxide shell nanocomposite: versatile magnetic matrix for anionic functional materials. Angew Chem Int Edit 2009;48:5888–92.
[96] Zhu MS, Sun ZC, Fujitsuka M, Majima T. Z-scheme photocatalytic water splitting on a 2D heterostructure of black phosphorus/bismuth vanadate using visible light. Angew Chem Int Edit 2018;57:2160–4.
[97] Gunjakar JL, Kim TW, Kim HN, Kim IY, Hwang SJ. Mesoporous layer-by-layer ordered nanohybrids of layered double hydroxide and layered metal oxide: highly active visible light photocatalysts with improved chemical stability. J Am Chem Soc 2011;133:14998–5007.
[98] Szabo T, Veres A, Cho E, Khim J, Varga N, Dekany I. Photocatalyst separation from aqueous dispersion using graphene oxide/$TiO_2$ nanocomposites. Colloid Surf A 2013;433:230–9.
[99] Patzko A, Kun R, Hornok V, Dekany I, Engelhardt T, Schall N. ZnAl-layer double hydroxides as photocatalysts for oxidation of phenol in aqueous solution. Colloid Surf A 2005;265:64–72.
[100] Boppella R, Choi CH, Moon J, Kim DH. Spatial charge separation on strongly coupled 2D-hybrid of rGO/La2Ti2O7/NiFe-LDH heterostructures for highly efficient noble metal free photocatalytic hydrogen generation. Appl Catal B Environ 2018;239:178–86.
[101] Mallakpour S, Hatami M. LDH-VB9-$TiO_2$ and LDH-VB9-$TiO_2$/crosslinked PVA nanocomposite prepared via facile and green technique and their photo-

degradation application for methylene blue dye under ultraviolet illumination. Appl Clay Sci 2018;163:235–48.
[102] Rossi LM, Costa NJS, Silva FP, Wojcieszak R. Magnetic nanomaterials in catalysis: advanced catalysts for magnetic separation and beyond. Green Chem 2014;16:2906–33.
[103] Goodman ED, Zhou CS, Cargnello M. Design of organic/inorganic hybrid catalysts for energy and environmental applications. ACS Central Sci 2020;6:1916–37.
[104] Xie ZK, Liu ZC, Wang YD, Yang QH, Xu LY, Ding WP. An overview of recent development in composite catalysts from porous materials for various reactions and processes. Int J Mol Sci 2010;11:2152–87.
[105] Parlett CMA, Wilson K, Lee AF. Hierarchical porous materials: catalytic applications. Chem Soc Rev 2013;42:3876–93.
[106] Zong YT, Li KT, Tian R, Lin YJ, Lu C. Highly dispersed layered double oxide hollow spheres with sufficient active sites for adsorption of methyl blue. Nanoscale 2018;10:23191–7.
[107] Hu QH, Xu ZP, Qiao SZ, Haghseresht F, Wilson M, Lu GQ. A novel color removal adsorbent from heterocoagulation of cationic and anionic clays. J Colloid Interface Sci 2007;308:191–9.
[108] Gong JM, Liu T, Wang XQ, Hu XL, Zhang LZ. Efficient removal of heavy metal ions from aqueous systems with the assembly of anisotropic layered double hydroxide nanocrystals@carbon nanosphere. Environ Sci Technol 2011;45:6181–7.
[109] Zhang B, Hu RT, Sun DJ, Wu T, Li YJ. Fabrication of magnetite-graphene oxide/MgAI-layered double hydroxide composites for efficient removal of emulsified oils from various oil-in-water emulsions. J Chem Eng Data 2018;63:4689–702.
[110] Zubitur MM, Sudol ED, Dimonie VL, El-Aasser MS. Monodisperse micron-size polymer core/nanoparticle pigment shell composite particles via heteroaggregation. J Appl Polym Sci 2009;114:264–74.
[111] Lee JH, Mahmoud MA, Sitterle VB, Sitterle JJ, Meredith JC. Highly scattering, surface-enhanced Raman scattering-active, metal nanoparticle-coated polymers prepared via combined swelling-heteroaggregation. Chem Mater 2009;21:5654–63.
[112] Deak A, Janovak L, Tallosy SP, Bito T, Sebok D, Buzas N, et al. Spherical LDH-$Ag^{0}$-montmorillonite heterocoagulated system with a pH-dependent sol-gel structure for controlled accessibility of AgNPs immobilized on the clay lamellae. Langmuir 2015;31:2019–27.
[113] Liu Y, Wu Y, Zhang R, Lam J, Ng JC, Xu ZP, et al. Investigating the use of layered double hydroxide nanoparticles as carriers of metal oxides for theranostics of ROS-related diseases. ACS Appl Bio Mater 2019;2:5930–40.
[114] Darabdhara G, Bordoloi J, Manna P, Das MR. Biocompatible bimetallic au-Ni doped graphitic carbon nitride sheets: a novel peroxidase-mimicking artificial enzyme for rapid and highly sensitive colorimetric detection of glucose. Sens Actuator B Chem 2019;285:277–90.
[115] Zhao XJ, Mai ZB, Kang XH, Zou XY. Direct electrochemistry and electrocatalysis of horseradish peroxidase based on clay-chitosan-gold nanoparticle nanocomposite. Biosens Bioelectron 2008;23:1032–8.
[116] Soh N, Kaneko S, Uozumi K, Ueda T, Kamada K. Preparation of an enzyme/inorganic nanosheet/magnetic bead complex and its enzymatic activity. J Mater Sci 2014;49:8010–5.
[117] Gunawan P, Xu R. Direct assembly of anisotropic layered double hydroxide (LDH) nanocrystals on spherical template for fabrication of drug-LDH hollow nanospheres. Chem Mater 2009;21:781–3.
[118] Peng EW, Choo ESG, Chandrasekharan P, Yang CT, Ding J, Chuang KH, et al. Synthesis of manganese ferrite/graphene oxide nanocomposites for biomedical applications. Small 2012;8:3620–30.
[119] Han YW, Liu N, Wang N, He ZH, Liu QC. Assembly of Ni-Al layered double hydroxide and oxide graphene quantum dots for supercapacitors. J Mater Res 2018;33:4215–23.
[120] Bai Y, Xing Z, Yu H, Li Z, Amal R, Wang LZ. Porous titania nanosheet/nanoparticle hybrids as photoanodes for dye-sensitized solar cells. ACS Appl Mater Interfaces 2013;5:12058–65.
[121] Kim JM, Cho Y, Guccini V, Hahn M, Yan BY, Salazar-Alvarez G, et al. TEMPO-oxidized cellulose nanofibers as versatile additives for highly stable silicon anode in lithium-ion batteries. Electrochim Acta 2021;369:137708.
[122] Wang YL, Wang ZC, Rui YP, Li MG. Horseradish peroxidase immobilization on carbon nanodots/CoFe layered double hydroxides: direct electrochemistry and hydrogen peroxide sensing. Biosens Bioelectron 2015;64:57–62.
[123] Amjadi M, Hallaj T, Kouhi Z. An enzyme-free fluorescent probe based on carbon dots - MnO2 nanosheets for determination of uric acid. J Photochem Photobiol A Chem 2018;356:603–9.
[124] Dong BL, Li HF, Sun JF, Mari GM, Yu XZ, Ke YB, et al. Development of a fluorescence immunoassay for highly sensitive detection of amantadine using the nanoassembly of carbon dots and MnO2 nanosheets as the signal probe. Sens Actuator B Chem 2019;286:214–21.
[125] He DG, Yang XX, He XX, Wang KM, Yang X, He X, et al. A sensitive turn-on fluorescent probe for intracellular imaging of glutathione using single-layer $MnO_2$ nanosheet-quenched fluorescent carbon quantum dots. Chem Commun 2015;51:14764–7.
[126] Sternitzke M. Structural ceramic nanocomposites. J Eur Ceram Soc 1997;17:1061–82.
[127] Madhavan N, Mukherjee M, Basavaraj MG. Porous ceramics via processable Pickering emulsion stabilized by oppositely charged colloids. Langmuir 2020;36:11645–54.
[128] Munoz M, Cerbelaud M, Videcoq A, Saad H, Boulle A, Meille S, et al. Nacre-like alumina composites based on heteroaggregation. J Eur Ceram Soc 2020;40:5773–8.
[129] Fan JP, Zhao DQ, Xu ZN, Wu MS. Preparation of MWNTS/$Al_2O_3$ composites and their mechanical and electrical properties. Sci China Ser E Technol Sci 2005;48:622–31.
[130] Kazmierczak-Balata A, Mazur J. Effect of carbon nanoparticle reinforcement on mechanical and thermal properties of silicon carbide ceramics. Ceram Int 2018;44:10273–80.